# An experimental and theoretical investigation of electrostatic suppression of the Leidenfrost state

Yi Lu [a,b,*], Jiming Bao [c], Dong Liu [a,*]

[a] *Department of Mechanical Engineering, University of Houston, Houston, TX, 77204-4006, USA*
[b] *Guangdong Provincial Key Laboratory of Optical Information Materials and Technology & Institute of Electronic Paper Displays, South China Academy of Advanced Optoelectronics, South China Normal University, Guangzhou 510006, China*
[c] *Department of Electrical and Computer Engineering, University of Houston, Houston, TX, 77204-4006, USA*

**ARTICLE INFO**

**ABSTRACT**

The formation of a thermally insulating vapor layer at the Leidenfrost state poses a major concern for heat transfer performance and safety operation of many phase change thermal systems. It is desirable to develop effective means to suppress the Leidenfrost state and to elevate the Leidenfrost point (LFP). In this work, the electrostatic suppression of a Leidenfrost drop was investigated by using a combined experimental and analytical approach. The effects of the voltage and driving frequency of the electric field on the LFP were measured. A theoretical model based on the electromechanical force balance and the Kelvin-Helmholtz instability analysis was formulated to quantify the relationship between the LFP and the applied electric field. This approach overcomes the major drawbacks of the existing models in the literature by offering a direct prediction of the LFP for a wide range of fluid types (electrically conducting or dielectric) enhanced by either DC or AC field.

## 1. Introduction

A liquid drop at the Leidenfrost state is levitated over a superheated surface by a thin vapor layer that arises from rapid evaporation at the bottom of the drop. Since direct liquid-solid contact is deprived, heat transfer between the drop and the substrate is primarily via conduction through the vapor layer, making the Leidenfrost state very ineffective for thermal energy transport. It is thus crucial to suppress or delay the occurrence of Leidenfrost state in order to ensure the performance of a myriad of liquid drop-based applications such as spray cooling, spray quenching, liquid fire extinguishing and fuel injection [1–7]. Besides, the Leidenfrost state is also encountered in bulk boiling when the critical heat flux (CHF) condition is exceeded. It demarcates the complete transition of heat transfer regime from the preferred nucleate boiling to the least effective film boiling, and often precedes the catastrophic boiling crisis [8,9]. Therefore, a good grasp of the key processes and suppression mechanisms of the Leidenfrost state will help to improve the fundamental understanding of the boiling crisis and devise new strategy to enhance CHF [10–12].

Suppression of the Leidenfrost state can be achieved by elevating the threshold temperature at which it commences, also known as the Leidenfrost point (LFP). Surface properties, such as surface wettability and roughness, have a significant impact on the LFP. Hydrophilic surfaces, either inherent or chemically modified, generally favor a higher LFP than their hydrophobic counterparts, since the surface affinity to liquids facilitates rewetting at the dry-out conditions [13–17]. Recently, engineered surfaces with artificial micro- or nanostructures have been shown to enhance the LFP drastically [18,19] and the degree of enhancement well exceeds the improvement due to the wettability change by surface roughness alone. Microscale surface structures usually take the form of micropillars. The pillar height is comparable to the typical vapor layer thickness (10 ~ 100 $\mu$m) [20–25] so that the micropillars are able to perforate through the vapor layer to restore the liquid-solid contact [9,26,27]. In close spacing, the microstructures also produce capillary wetting to redraw liquid to the hot surface, which is beneficial for lifting the LFP. However, compared to a plain surface, the microstructures cause more vapor generation owing to the enlarged total heat transfer area, and their presence blocks the flow path of the vapor release to the ambient [21,23]. Their dimensions and layout must be carefully designed to optimize the LFP enhancement. Nanoscale surface structures, such as nanorods and nanowires [28–33], on the other hand, are more promising as they do not suffer from the major drawbacks of the microstructures. Nanostructures induce strong capillary wicking or hemi-wicking effect to keep the solid surface from drying out at high temper-

* Corresponding author.
*E-mail addresses:* yilu@m.scnu.edu.cn (Y. Lu), dongliu@uh.edu (D. Liu).

atures [34–38] and are shown to even trigger explosive heterogeneous boiling at the hot surface which makes it impossible for a stable vapor layer to survive as in the Leidenfrost state [39]. On nanoporous surfaces, vapor phase evaporated from the drop percolates into the porous matrix, effectively reducing the vapor layer thickness [40–42]. It has been demonstrated that the LFP of water drops is elevated by 100 °C to 140 °C on micro/nanostructured surfaces above that on a plain surface [43]. More recently, hierarchical surfaces with both micro- and nanostructures have been adopted to further enhance the LFP [35,39,43–45]. The rationale is that the microstructures will recreate the liquid-solid contact and the nanostructures induce capillary wicking. The LFP was shown to increase to 453 °C for a water drop on a nanoporous surface decorated with micropillars [39], and no Leidenfrost state was observed at 570 °C on a hierarchical surface consisting of a superhydrophilic nanomembrane anchored on the top of a micropillar array [45].

While micro/nanostructured surfaces are highly effective in enhancing the LFP, they suffer from some drawbacks common for functionalized surfaces, e.g., complex and costly to manufacture, susceptible to fouling, difficult to scale up, and lacking structural durability. To address these issues, active enhancement approaches using external stimulus have been attempted. One example is the introduction of mechanical vibrations for Leidenfrost suppression. A vibrating plate driven by a low-frequency (~$10^2$ Hz) loudspeaker was used to generate a collision force in the Leidenfrost drop, causing the vapor layer to diminish till it broke down [46]. Alternatively, a high-frequency (~$10^5$ Hz) acoustic field was excited in the Leidenfrost drop to produce surface capillary waves. By tuning the acoustic amplitude and frequency, the capillary waves destabilize the liquid-vapor interface and regenerate the direct contact between the drop and the solid surface. It was shown that the surface temperature reduces to 45% below the LFP at the Leidenfrost condition [47].

Active LFP enhancement can also be achieved by utilizing the electric field. This approach is more attractive for it requires no moving parts and is ultralow in power consumption. Typically, a direct current (DC) or alternating current (AC) voltage is applied between the Leidenfrost drop and the substrate to create a strong electric field concentrated across the thin vapor layer (~10 V/$\mu$m). An electrostatic attraction force is then induced to pull the drop toward the hot surface. As a result, the vapor layer is suppressed. Using a low-frequency AC signal ($f$ = 0.5 Hz and $V$ = 40 V), it was first demonstrated in [48] that the Leidenfrost state for a water drop was suppressed at a surface temperature at 280°C. A theoretical model, based on the balance between the vapor pressure force, drop weight and electrostatic force, was developed to determine the minimum (threshold) voltage to attain the Leidenfrost suppression. In another study [49], DC-voltage-induced Leidenfrost suppression was achieved at surface temperatures of up to 550 °C. A similar force balance model was formulated to predict the threshold voltage, which included more details of conduction, convection and radiation heat transfer as well as the effect of the vapor layer on the total electrical capacitance of the drop-substrate system. Later, the liquid fingering phenomenon was observed at the bottom of the Leidenfrost drop in the presence of an applied DC voltage [50]. The liquid fingers, originating from undulations at the liquid-vapor interface and amplified by the electric field, will bridge the vapor layer and destabilize the Leidenfrost state if the DC voltage exceeded a critical value. To explore the underlying physics, the dynamics of the vapor layer thickness was modeled by solving the thin-film lubrication equation, based on which the linear instability theory was applied to derive the instability criterion and the minimum voltage required to subdue the Leidenfrost state. More recently, the effect of AC electric field was investigated experimentally by the same group [51]. It was found that the effectiveness of AC field for Leidenfrost suppression was negated be-

yond certain high frequencies, since the electric field will penetrate inside the electrolyte drop even though it is inherently conductive, causing the destabilizing electric force to weaken.

The foregoing research has shed important light on various aspects of Leidenfrost suppression by electric field and, in particular, provided the theoretical framework to rationalize the suppression mechanisms. However, several critical drawbacks exist. First, as will be shown later, the force balance model implies that, due to different scaling relationships with respect to the vapor layer thickness, the electric force will be outpaced by the stabilizing viscous pressure force as the vapor layer diminishes. Thus, the Leidenfrost drop would persist regardless of the magnitude of the applied field. In other words, the force balance model alone is inadequate to elucidate the Leidenfrost suppression observed in experiments. Second, the distribution of the electric field is required in any theoretical model for Leidenfrost suppression. While all existing models assume the electric field is completely confined in the vapor layer, it is only valid for Leidenfrost drops of electrically conducting liquid under the modulation of DC field. When a dielectric fluid is used and/or an AC field is applied, the penetration of the electric field into the interior of the liquid drop will drastically change the field distribution. Hence it is dubious if the conclusions derived from the existing models can be applied directly to Leidenfrost suppression for general heat transfer fluids, such as refrigerants. Lastly, for any thermal system that may undergo the Leidenfrost state, it is highly desirable to be able to predict the LFP for given conditions (such as the liquid type and the electric field). Unfortunately, no explicit predictions are yet available from the existing models.

It is the aim of this work to address these issues and fill the knowledge gap in the current understanding of the Leidenfrost suppression processes through a combined experimental and theoretical study. The LFP of water drops under the influence of both DC and AC fields was measured and a synchronized high-speed optical imaging and infrared (IR) thermography approach was employed to characterize the thermohydraulic behaviors of the Leidenfrost drop. A new analytical model was developed that first deduced the relationship between the wall superheat, the electric field and the vapor layer thickness from the force balance model and then derived an instability criterion for the Leidenfrost suppression by applying the Kelvin-Helmholtz instability analysis. This model is capable of providing direct predictions of the LFP for any liquid, conducting or dielectric, under either DC or AC field. Reversely, the threshold frequency and magnitude of the electric field needed to subdue the Leidenfrost state at any given surface temperature can also be estimated. Finally, the model predictions were validated with the experimental data.

## 2. Experimental methods

### 2.1. Experimental setup

The experimental apparatus is shown schematically in Fig. 1. It consists of the test piece, the power supply, the electrical signal control system, and the synchronized high-speed optical and IR thermographic imaging system. The test piece was made of a 385-$\mu$m-thick 3" silicon wafer (Silicon Quest) with a 100-nm-thick, thermally grown silicon dioxide ($SiO_2$) layer on both sides. The silicon substrate worked directly as the ground electrode of the electrical circuit of the drop-solid system. A chromium (Cr) thin-film heater was fabricated on the backside of the test piece. It was powered by a DC power supply (N5771A, Agilent) to provide the wall superheat necessary to produce the Leidenfrost state.

In the Leidenfrost experiments, a deionized water drop of an initial volume $\Lambda$ = 20.0 $\pm$ 0.1 $\mu$L was used as the test target. The initial drop size (radius $R_0$ = 1.68 mm) was smaller than the cap-
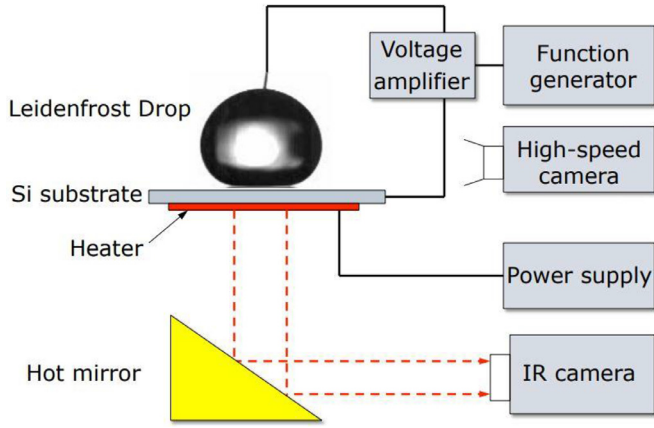
**Fig. 1.** Experimental apparatus for electrostatic suppression of the Leidenfrost state.

illary length $l_c$ $(= \sqrt{\sigma_{lv}/(\Delta \rho g)} = 2.5$ mm, where $\sigma_{lv}$ is the surface tension of the water-air interface and $\Delta \rho$ is the density difference between water and air) such that a spherical cap geometry can be assumed. Meanwhile, the drop size was large enough to allow sufficient evaporation time to make proper experimental measurements. At each experiment, the water drop was gently deposited by a micropipette onto the test surface from a height of $h = 1$ mm above. The corresponding Weber number ($We = \rho U^2 D/\sigma$, where $U$ is the impact velocity of the drop and $D$ is the drop diameter) was very small ($We = 1.07$) that the drop impact had a negligible influence on the Leidenfrost effect. A 99.99% pure platinum wire of a 100-μm diameter was attached to the tip of the micropipette to guide the drop dispensing and remained inserted into the drop throughout the experiment. The wire served as the ground electrode and also helped to confine the lateral motion of the drop at the Leidenfrost state.

The DC and AC signals for the Leidenfrost state suppression were produced by an arbitrary function generator (Fluke 294-U, Fluke) in combination with an inverting amplifier (BOP 200-1D-BIT 4886, KEPCO). The DC voltage was varied between 56 V and 140 V. The AC signal, $V(t)$, followed a sinusoidal waveform (unless otherwise specified) in this study

$$V(t) = V_0 \cos(2\pi f_E t) \tag{1}$$

where $V_0$ and $f_E$ are the amplitude and frequency of the applied signal and $t$ is time. For the results reported in this paper, the root mean square (RMS) value of the AC voltages was set as $V_{RMS} = \frac{1}{\sqrt{2}} V_0 = 56$ V and $f_E$ ranged from 1 Hz to 100 kHz. One exception is noted when observing the response of a Leidenfrost drop to a train of step-function voltage signals, where a 50% duty cycle square pulse wave was applied (the details will be discussed in Section 4.1).

### 2.2. Measurement techniques

The Leidenfrost temperature was determined by the drop lifetime method, in which the evaporation time of a drop of a given initial volume was measured over a range of preset wall surface temperatures. The LFP was deemed as the one corresponding to the longest evaporation time [52]. The drop evaporation time was obtained from the video recordings of the evaporation process, defined as the time interval between the moment the drop was deposited onto the surface and the moment the drop was completely vaporized. Since the evaporation process may last as long as ~ 120 seconds, the frame rate and resolution of the optical camera were varied, according to the evaporation regime the drop was subject to at a specific surface temperature, to capture the entire course.

The measurement accuracy depends mainly on how well the drop morphology can be distinguished at the last moment of evaporation. As the drop deforms violently in the contact/transition boiling regime, especially right before reaching the Leidenfrost state, the largest measurement uncertainty (~0.6 seconds) is expected near the LFP. This is significantly smaller than the measured drop lifetime and, therefore, will not affect the determination of the LFP.

A synchronized optical imaging and IR thermography approach was used to observe the Leidenfrost drop motion and measure the wall surface temperature simultaneously [53]. The drop motion was recorded at 6000-10000 frame per second (fps) by a high-speed camera (FASTCAM Ultima APX, Photon) together with a Nikon micro-lens (f 2.8). The pixel resolution ranged from 17.1 μm to 33.5 μm, depending on the distance between the lens and the drop. The shutter speed was set to 1/16000 s, and a cold light illumination source was used to compensate for the short exposure time. The wall temperature of the heater side of the test piece was measured by an IR camera (SC 7650, FLIR). The maximum resolution was 640 × 512 pixels with a spatial resolution of 150 μm/pixel. The maximum frame rate used was 180 fps. To facilitate the IR measurement, a water-based black paint was sprayed on the heater surface to yield an emissivity of $\varepsilon_h$ ~ 0.97. Due to the limitation of space, a gold-coated hot mirror (N-BK7, Edmund Optics) was used to re-direct the thermal radiation from the heater to the IR camera, as shown in Fig. 1. The wall temperature of the evaporation surface was then acquired after considering heat conduction through the thickness of the silicon wafer. The overall uncertainty in the temperature measurement was ± 1 °C. Based on the temperature distribution, the local heat flux was computed by solving the energy balance equation for each volume element of the substrate. The detailed data deduction can be found in [54]. A pulse generator (BNC 565, Berkeley Nucleonics) was used to synchronize the optical and the IR cameras.

## 3. Theoretical models

### 3.1. Force balance model

Dynamics of the Leidenfrost drop can be analyzed by considering the force balance on the drop (as illustrated in Fig. 2)

$$m\frac{d^2\delta}{dt^2} = F_g + F_e - F_v - F_r \tag{2}$$

where $m$ is the mass of the drop, $\delta$ is the vapor layer thickness, $F_g$ is the drop weight ($F_g = mg$), $F_e$ is the electrostatic force of attraction when an electric field is applied, $F_v$ is the viscous pressure force in the vapor layer, and $F_r$ is the vapor recoil force on the liquid-vapor interface due to the momentum of evaporated vapor molecules. The solution of Eq. (2) will yield the temporal variation of $\delta$, the key marker for the drop motion and the viability of the Leidenfrost state. It will be shown that the force balance model alone is inadequate to fully capture the physics of electrical suppression, however, it provides the basis for the subsequent Kelvin-Helmholtz stability analysis.

### 3.1.1. Viscous pressure force

The viscous pressure force, $F_v$, arises when the evaporated vapor phase flows through the gap space between the drop and the surface. At the LFP, $F_v$ is strong enough to counter the weight of the drop[1] and keep the drop levitated. Using the cylindrical coordinates shown in Fig. 2, the viscous pressure force acting on the

---

[1] Since the Weber number is very small in this work, the effects of the dynamic pressure and the water hammer pressure of the drop are negligible.
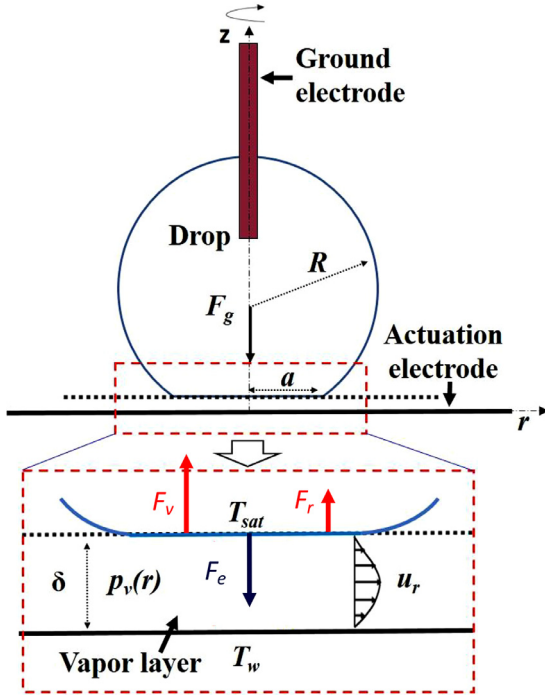
**Fig. 2.** Forces acting on the liquid-vapor interface of a Leidenfrost drop.

liquid drop can be calculated from

$$F_v = \int_0^a (p_v(r) - p_0) \cdot (2\pi r) \cdot dr \tag{3}$$

where $p_v(r)$ is the local pressure in the vapor layer, $p_0$ is the ambient pressure, and $a$ is the radius of the liquid-vapor interface at the bottom of the drop (also termed the *apparent contact radius* of the drop on the solid substrate, which will be defined in Section 3.1.3). In Eq. (3), $p_v(r)$ must be known in order to evaluate $F_v$.

The vapor flow originates from evaporation at the bottom of the drop. The rate of vapor generation is obtained by relating the vaporization energy to the heat conduction through the vapor layer [55–57]

$$\frac{dm}{dt} = \pi a^2 \left( \frac{k_v}{h_{lv}} \frac{\Delta T}{\delta} \right) \tag{4}$$

where $h_{lv}$ is the latent heat of evaporation, $k_v$ is thermal conductivity of vapor, and $\Delta T$ ($= T_w - T_{sat}$) is the difference between the surface temperature $T_w$ and the liquid saturation temperature $T_{sat}$. The vapor phase passes through the liquid-vapor interface with a relative velocity $\frac{1}{\rho_v \pi a^2} \frac{dm}{dt}$ while the interface itself moves at an instantaneous velocity $\frac{d\delta}{dt}$. Thus, the absolute velocity of the vapor phase $v_{z=\delta}$ is

$$v_{z=\delta} = \frac{1}{\rho_v \pi a^2} \frac{dm}{dt} - \frac{d\delta}{dt} = \frac{k_v}{\rho_v h_{lv}} \frac{\Delta T}{\delta} - \frac{d\delta}{dt} \tag{5}$$

Assuming the vapor flow is laminar, the continuity and momentum equations are [58]

$$\frac{\partial (ur)}{\partial r} + \frac{\partial (vr)}{\partial z} = 0 \tag{6}$$

$$\rho_v u \frac{\partial u}{\partial r} + \rho_v v \frac{\partial u}{\partial z} = -\frac{dp_v}{dr} + \mu_v \frac{\partial^2 u}{\partial z^2} \tag{7}$$

where $u$ and $v$ are the radial and axial velocity components, and $\rho_v$ and $\mu_v$ are the density and viscosity of vapor. The boundary

conditions are

$$u(r, 0) = 0, u(r, \delta) = 0, \ v(r, 0) = 0 \text{ and } v(r, \delta) = v_{z=\delta} \tag{8}$$

Since $\delta$ is very small ($\delta << a$), it is reasonable to assume $\frac{\partial u}{\partial r} \ll \frac{\partial u}{\partial z}$. Integrating Eqs. (6) and (7) from $z = 0$ to $z = \delta$ and applying the boundary conditions yield

$$\int_0^\delta \frac{\partial}{\partial r} (ur) dz + r v_{z=\delta} = 0 \tag{9}$$

$$\int_0^\delta \frac{1}{r} \frac{\partial}{\partial r} (\rho_v r u^2) dz = -\delta \left( \frac{dp_v}{dr} \right) + \mu_v \left( \frac{\partial u}{\partial z} \right)_{z=\delta} - \mu_v \left( \frac{\partial u}{\partial z} \right)_{z=0} \tag{10}$$

A parabolic profile is assumed for $u$ [58], which follows

$$u = 6u_m \left( \frac{z}{\delta} - \frac{z^2}{\delta^2} \right) \tag{11}$$

where $u_m$ is the mean vapor velocity defined as

$$u_m = \frac{1}{\delta} \int_0^\delta u \, dz \tag{12}$$

Then, combining Eq. (9) with Eqs. (5), (11) and (12), it leads to

$$u_m = \frac{r}{2\delta} \left( \frac{k_v}{\rho_v h_{lv}} \frac{\Delta T}{\delta} - \frac{d\delta}{dt} \right) \tag{13}$$

Substituting Eqs. (11) and (12) into the momentum equation Eq. (10), an equation is derived for the vapor pressure variation

$$\left( \frac{dp_v}{dr} \right) = -\frac{6}{\delta^3} \left( \frac{k_v}{\rho_v h_{lv}} \frac{\Delta T}{\delta} - \frac{d\delta}{dt} \right) \left[ \mu_v + \frac{3}{4} \rho_v \delta \left( \frac{k_v}{\rho_v h_{lv}} \frac{\Delta T}{\delta} - \frac{d\delta}{dt} \right) \right] r \tag{14}$$

Then, $p_v$ can be solved by integrating Eq. (14) in conjunction with the boundary condition $p_v(r = a) = p_0$

$$p_v - p_0 = \frac{3}{\delta^3} \left( \frac{k_v}{\rho_v h_{lv}} \frac{\Delta T}{\delta} - \frac{d\delta}{dt} \right)$$
$$\times \left[ \mu_v + \frac{3}{4} \rho_v \delta \left( \frac{k_v}{\rho_v h_{lv}} \frac{\Delta T}{\delta} - \frac{d\delta}{dt} \right) \right] (a^2 - r^2) \tag{15}$$

As a consequence, the upward pressure force is calculated as

$$F_v = \int_0^a (p_v - p_0) \cdot (2\pi r) \cdot dr = \frac{3\pi a^4}{2\delta^3} \left( \frac{k_v}{\rho_v h_{lv}} \frac{\Delta T}{\delta} - \frac{d\delta}{dt} \right)$$
$$\times \left[ \mu_v + \frac{3}{4} \rho_v \delta \left( \frac{k_v}{\rho_v h_{lv}} \frac{\Delta T}{\delta} - \frac{d\delta}{dt} \right) \right] \tag{16}$$

It is worth noting that $F_v$ scales inversely proportional to $\delta^4$.

### 3.1.2. Vapor recoil force

When a liquid evaporates, the vapor phase leaves with a higher velocity than the incoming liquid and leads to the vapor recoil force, $F_r$, also known as the evaporation momentum force [59]. For a Leidenfrost drop levitating over a thin vapor layer, the recoil force is regarded as an upward force to support the liquid's suspension. Considering the momentum conservation at the liquid-vapor interface, the recoil force is expressed as [60]

$$F_r = \eta^2 A \left( \frac{1}{\rho_v} - \frac{1}{\rho_l} \right) \tag{17}$$

where $A$ is the interface area and $\eta$ is the evaporation rate per unit interface area [61]. According to the foregoing definitions, it is easy to see $A = \pi a^2$ and $\eta = \frac{1}{\pi a^2} \frac{dm}{dt} = \frac{k_v}{h_{lv}} \frac{\Delta T}{\delta}$.
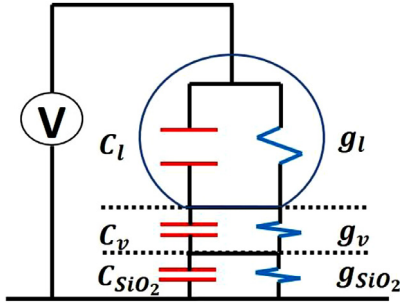
**Fig. 3.** Schematic of the RC model for the Leidenfrost drop-solid substrate system.
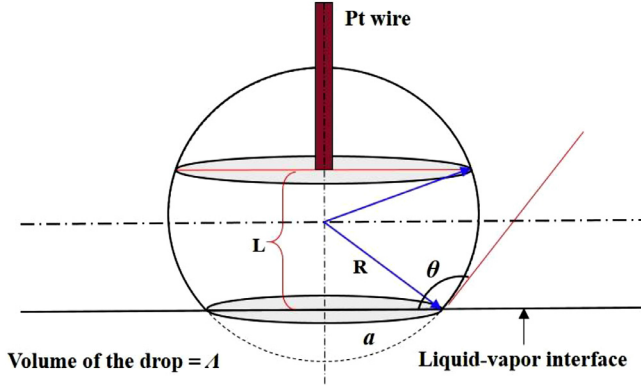


**Fig. 4.** Geometry of a Leidenfrost drop.

### 3.1.3. Electrical force

When a voltage is applied between the solid substrate and the Leidenfrost drop, the drop will remain equipotential if the liquid is electrically conducting and the electric field falls entirely across the vapor layer. The drop-substrate system can be modeled reasonably as a parallel plate capacitor with two armatures (the drop and the substrate) separated by a vapor layer. The electric force $F_e$ on the drop is interpreted as the electrostatic attraction between the two armatures. However, this model becomes problematic if the liquid is electrically insulating or when an AC voltage is used. In either case, the electric field will penetrate into the drop and the dielectric behavior of the liquid must be considered. To acquire a realistic estimate of the electric field distribution, a resistive-capacitive (RC) circuit model is employed [62]. As shown in Fig. 3, all the materials are each modeled as a resistor in parallel with a capacitor.

In order to find the electrical resistance $R$ and the capacitance $C$ of the drop-substrate system, it is important to specify the geometry of the Leidenfrost drop shown in Fig. 4. The equivalent radius of the drop is first deduced from the initial volume, $\Lambda$

$$R = \left(\frac{3\Lambda}{4\pi}\right)^{1/3} \tag{18}$$

Then, balancing the drop's weight and the Laplace pressure force yields the apparent contact radius, $a$ [63]

$$a = \frac{R^2}{l_c} \tag{19}$$

where $l_c$ is the capillary length defined earlier. Due to the existence of the vapor layer, the concept of contact angle is no longer applicable. Instead, the apparent contact angle, $\theta$, is used

$$\theta = \pi - \sin^{-1}\frac{a}{R} \tag{20}$$

Another parameter is the distance $L$ between the tip of the wire and the heating surface, which is controlled by the insertion depth

**Table 1**
Relative permittivity and conductivity of different materials.

| | | Dielectric constant | | Electrical conductivity (S/m) |
|---|---|---|---|---|
| Liquid water | $\varepsilon_l$ | 55.6 | $\sigma_l$ | $2 \times 10^{-4}$ |
| Water vapor | $\varepsilon_v$ | 1 | $\sigma_v$ | $5 \times 10^{-15}$ |
| $SiO_2$ | $\varepsilon_{SiO_2}$ | 3.9 | $\sigma_{SiO_2}$ | $1 \times 10^{-15}$ |

of the wire. When the wire just touches the apex of the drop, $L = R + \sqrt{R^2 - a^2}$.

With all the geometric parameters known, the resistance of the drop is given by [64]

$$R_l = \frac{1}{2\pi\sigma_l R}\ln\left[\frac{(R + R\cos\theta + L)(1 - \cos\theta)}{(R - R\cos\theta - L)(1 + \cos\theta)}\right] \tag{21}$$

where $\sigma_l$ is the electrical conductivity of the liquid. The capacitance is

$$C_l = f(\theta)\varepsilon_0\varepsilon_l R \tag{22}$$

where $\varepsilon_0$ is the permittivity in vacuum, $\varepsilon_l$ is the dielectric constant of the liquid, and $f(\theta)$ is the shape factor $f = 0.0592 + 0.0012\theta + 0.0022\tan(1.71 - \theta)$ [65]. The resistances and capacitances of the vapor layer and $SiO_2$ layer are

$$R_v = \frac{\delta}{\sigma_v A} \quad C_v = \varepsilon_0\varepsilon_v\frac{A}{\delta} \tag{23}$$

$$R_{SiO_2} = \frac{\delta_{SiO_2}}{\sigma_{SiO_2}A} \quad C_{SiO_2} = \varepsilon_0\varepsilon_{SiO_2}\frac{A}{\delta_{SiO_2}} \tag{24}$$

The electrical properties of the different materials involved are summarized in Table 1 [66,67].

When an AC voltage is applied, Eq. (1) can be rewritten in the phasor form

$$V(t) = \text{Re}\left[\sqrt{2}V_{RMS}e^{jwt}\right] \tag{25}$$

where the angular frequency is $\omega = 2\pi f_E$, $j = \sqrt{-1}$, and $\text{Re}[\cdot]$ represents the real part of a complex quantity. Accordingly, the impedance of a single component of the RC circuit is

$$Z_n = \frac{R_n}{1 + j\omega R_n C_n} \tag{26}$$

where the subscript $n$ can be "$l$" for liquid, "$v$" for vapor, and "$SiO_2$" for $SiO_2$. The equivalent impedance of the entire RC circuit is

$$Z_{eq} = \sum Z_n = Z_l + Z_v + Z_{SiO_2} \tag{27}$$

Subsequently, the electric field distributions in the vapor layer and the liquid drop are [62]

$$E_v = \text{Re}\left[\frac{Z_v}{Z_{eq}}\frac{V}{\delta}\right] = \frac{\left(\frac{R_v}{1+\omega^2 C_v^2 R_v^2}\right)\left(\sum\frac{R_n}{1+\omega^2 C_n^2 R_n^2}\right) + \left(\frac{C_v R_v^2 \omega}{1+\omega^2 C_v^2 R_v^2}\right)\left(\sum\frac{C_n R_n^2 \omega}{1+\omega^2 C_n^2 R_n^2}\right)}{\left(\sum\frac{R_n}{1+\omega^2 C_n^2 R_n^2}\right)^2 + \left(\sum\frac{C_n R_n^2 \omega}{1+\omega^2 C_n^2 R_n^2}\right)^2} \cdot \frac{V_0}{\delta} \tag{28}$$

$$E_l = \text{Re}\left[\frac{Z_l}{Z_{eq}}\frac{V}{L^*}\right] = \frac{\left(\frac{R_l}{1+\omega^2 C_l^2 R_l^2}\right)\left(\sum\frac{R_n}{1+\omega^2 C_n^2 R_n^2}\right) + \left(\frac{C_l R_l^2 \omega}{1+\omega^2 C_l^2 R_l^2}\right)\left(\sum\frac{C_n R_n^2 \omega}{1+\omega^2 C_n^2 R_n^2}\right)}{\left(\sum\frac{R_n}{1+\omega^2 C_n^2 R_n^2}\right)^2 + \left(\sum\frac{C_n R_n^2 \omega}{1+\omega^2 C_n^2 R_n^2}\right)^2} \cdot \frac{V_0}{L^*} \tag{29}$$

where $L^*$ is the electric penetration depth into the drop when the dielectric behavior of the liquid is considered and it can be shown that $L^* \approx \frac{A}{2\pi R}\ln[\frac{(R+R\cos\theta+L)(1-\cos\theta)}{(R-R\cos\theta-L)(1+\cos\theta)}]$. In the case of a conducting drop exposed to a DC field ($\omega = 0$), $E_l = (R_l/\sum R_n)\frac{V_0}{L^*} \approx 0$

**Table 2**
Scale analysis of different force terms in the force
balance equation.

| $\delta$ ($\mu$m) | $F_g$ (N) | $F_e$ (N) | $F_v$ (N) | $F_r$ (N) |
|---|---|---|---|---|
| 100 | $10^{-4}$ | $10^{-6}$ | $10^{-6}$ | $10^{-9}$ |
| 35 | $10^{-4}$ | $10^{-4}$ | $10^{-4}$ | $10^{-8}$ |
| 10 | $10^{-4}$ | $10^{-3}$ | $10^{-2}$ | $10^{-7}$ |
| 1 | $10^{-4}$ | $10^{-1}$ | $10^{2}$ | $10^{-5}$ |

and $E_v \approx (R_v / \sum R_n) \frac{V_0}{\delta}$, since $R_v > R_{SiO_2} \gg R_l$, i.e., the electric field is confined primarily in the vapor layer, just as expected. At very high frequencies, $E_v = [(1/C_v) / \sum (1/C_n)] \frac{V_0}{\delta}$, since $\sum (1/C_n) > (1/C_v)$ i.e., the system behaves as a pure capacitor and the electric field diminishes in the vapor layer.

After the electric field is determined, the electric stress $\overset{\leftrightarrow}{\tau}^E$ induced in a material is given by the Maxwell stress tensor

$$\overset{\leftrightarrow}{\tau}^E = \varepsilon_0 \varepsilon \left( \overset{\rightarrow}{E} \overset{\rightarrow}{E} - \frac{1}{2} E^2 \overset{\leftrightarrow}{I} \right) \tag{30}$$

At the liquid-vapor interface, the phase discontinuity (i.e., the jump in $\varepsilon$ across the interface) leads to an electric force $F_e$, which can be calculated by integrating the Maxwell stress tensor using the Gauss's pillbox method [68–70]

$$F_e = \left| \int_A \overset{\leftrightarrow}{\tau}^E \cdot \hat{n} dS \right| = \frac{1}{2} \varepsilon_0 \left( \varepsilon_v E_v^2 - \varepsilon_l E_l^2 \right) \cdot \pi a^2 \tag{31}$$

and the direction of $F_e$ always points to the vapor side of the interface. Combining Eqs. (28), (29) and (31), it is found that $F_e$ scales as $\sim 1/\delta^2$.

*3.1.4. Variation of vapor layer thickness*
Before all the force terms are included in Eq. (2), a scale analysis is performed to evaluate the relative significance of each component at different stages of the interface motion (represented by the $\delta$ values). The result in Table 2 reveals that as the vapor layer thickness decreases, the vapor recoil force $F_r$ is always a few orders of magnitude smaller than less than the electric force $F_e$ and the viscous pressure force $F_v$. Thus, it is neglected in the subsequent analysis.

Now, the force balance equation (Eq. (2)) transforms to

$$\rho_l \Lambda \frac{d}{dt} \left( \frac{d\delta}{dt} \right) = \rho_l g \Lambda + \frac{1}{2} \varepsilon_0 \left( \varepsilon_v E_v^2 - \varepsilon_l E_l^2 \right) \pi a^2 - \frac{3\pi a^4}{2\delta^3} \left( \frac{k_v}{\rho_v h_{lv}} \frac{\Delta T}{\delta} - \frac{d\delta}{dt} \right) \left[ \mu_v + \frac{3}{4} \rho_v \delta \left( \frac{k_v}{\rho_v h_{lv}} \frac{\Delta T}{\delta} - \frac{d\delta}{dt} \right) \right] \tag{32}$$

This is a second order ordinary differential equation with respect to the temporal variation of the vapor layer thickness, and it requires two initial conditions to solve. By assuming a sessile drop at $t = 0$, the first condition is

$$\frac{d\delta}{dt}(t = 0) = 0 \tag{33}$$

The second condition comes from the initial vapor thickness $\delta_0$ before the electric field is actuated, which can be computed by nulling the electric field and the time-dependent terms in Eq. (32)

$$\delta_0(t = 0) = \left[ \frac{\frac{3\pi}{2} \left( \frac{k_v \Delta T}{\rho_v h_{lv}} \right) \left[ \mu_v + \frac{3}{4} \left( \frac{k_v \Delta T}{h_{lv}} \right) \right]}{\rho_l g \Lambda} \right]^{1/4} a \tag{34}$$

For a 20.0 μL water drop residing on a superheated surface at $T_w = 300°$C, Eq. (34) yields $\delta_0 = 34.7$ $\mu$m. Using Eqs. (32)-(34), the dynamics of the vapor layer can be solved for different drop size, wall superheat and electric field. Ideally, the Leidenfrost state is deemed suppressed when the vapor layer thickness $\delta$ reduces to zero.

*3.2. Interfacial instability analysis*

From the force balance model, it has been deduced that $F_e \sim \frac{1}{\delta^2}$ and $F_v \sim \frac{1}{\delta^4}$, which indicates the stabilizing viscous pressure force will quickly dominate the destabilizing electric force as $\delta$ diminishes. Thus, the vapor layer will never vanish and the Leidenfrost state cannot be eliminated regardless of the applied field. This is an artifact inherent to all force balance models that clearly contradicts the experimental observations. To make the models useful, it is then necessary to choose some threshold value for the vapor layer thickness $\delta_{cr}$ and assert a successful Leidenfrost suppression when $\delta$ reduces to below $\delta_{cr}$. Unfortunately, the selection of $\delta_{cr}$ lacks scientific rigor and is often arbitrary, e.g., $\delta_{cr} = \delta_0/3$ was chosen in [49]. To circumvent this problem, the stability of a Leidenfrost drop was studied by solving the eigenvalue problem of the pressure disturbances emerging from the evolution equation of $\delta$ [50]. If the eigenvalues of the inverse time constant have a real part, the disturbances will grow in time and the Leidenfrost state is suppressed. The linear instability analysis is able to predict the critical voltage for Leidenfrost suppression for given drop size and surface temperature. However, its utility is restricted to conducting liquids in a DC field because the linearized evolution equation is only mathematically tractable when assuming the electric field falls entirely across the vapor layer. If Leidenfrost drops of insulating liquid are concerned or drops of conducting liquid are subject to an AC field, the electric field will diffuse into the interior of the drop, making the linear analysis invalid. Furthermore, the linear stability model does not automatically offer an explicit prediction of the LFP for given operating conditions, which is imperative for the safety design and performance evaluation of many practical phase change heat transfer devices. In this section, a Kelvin-Helmholtz instability analysis is presented in an effort to overcome the deficiencies of the existing models. It takes the relationship between the wall superheat, the electric field and the vapor layer thickness derived from the force balance model as the input, and provides a more comprehensive and versatile description of the Leidenfrost suppression mechanism as well as a direct prediction of the LFP.

The liquid-vapor interface of a Leidenfrost drop shares many features as that in film boiling, both bearing a continuous vapor layer of finite thickness over a superheated surface. Hence some

insights are first acquired from the extensive body of work on the instability analysis of film boiling. Most studies can be traced back to Taylor's pioneering work on hydrodynamic instabilities at an interface separating two fluids of different density [71]. The classical approach is that when the interface is disturbed, its stability is governed by the evolution of a representative perturbation wave

$$\eta(x, t) = \eta_0 e^{i(kx - st)} \tag{35}$$

where $\eta_0$ is the amplitude of the wave, $k$ is the wavenumber (which is related to the perturbation wavelength $\lambda$ by $k = 2\pi/\lambda$), and $s$ is the inverse time constant that dictates the growth rate of the wave. If $s$ is real, the perturbation wave will be periodic in time and, therefore, stable, whereas an imaginary solution of $s$ signifies the exponential growth of the perturbation. Over the years, the effects of surface tension, viscosity and evaporation heat transfer have been added in the analysis to reflect the particularity of film boiling. It is found that surface tension and evaporation stabilize the interfacial disturbances and viscosity does not eradicate an instability but merely slows its growth rate [72–77].

In the presence of an electric field, the electric stress $\overset{\leftrightarrow}{\tau}^E$, computed by Eq. (30), will arise at the liquid-vapor interface. It modifies the balance of normal stresses that must satisfy Laplace's condition otherwise. Following the analysis in [12,78–80], a dispersion relation between $s$ and $k$ can be derived

$$s^2 = \frac{\sigma_{lv}}{\rho_l + \rho_v}k^3 - \frac{(\rho_l - \rho_v)g}{\rho_l + \rho_v}k - \frac{f(E, \varepsilon_l, \varepsilon_v)}{\rho_l + \rho_v}k^2\coth(k\delta) \quad (36)$$

where $\sigma_{lv}$ is the liquid-vapor surface tension and $f(E, \varepsilon_l, \varepsilon_v)$ is a function expressed as

$$f(E, \varepsilon_l, \varepsilon_v) = \frac{\varepsilon_0\varepsilon_l(\varepsilon_l - \varepsilon_v)^2}{\varepsilon_v(\varepsilon_l + \varepsilon_v)}E_l^2 = \frac{\varepsilon_0\varepsilon_v(\varepsilon_l - \varepsilon_v)^2}{\varepsilon_l(\varepsilon_l + \varepsilon_v)}E_v^2 \quad (37)$$

According to Eq. (36), surface tension tends to increase $s^2$ and stabilize the liquid-vapor interface. On the other hand, the gravitational field and the electric field decrease $s^2$, making the interfacial disturbances more susceptible to growth. Further, it can be deduced that long-wavelength disturbances (small $k$) are unstable ($s^2 < 0$) while short-wavelength disturbances (large $k$) are stable ($s^2 > 0$). The critical wavenumber $k_c$ associated with waves of the fastest growth rate can be determined by solving $\frac{ds^2}{dk} = 0$. The corresponding wavelength $\lambda_c = \frac{2\pi}{k_c}$ is the most dangerous wavelength, i.e., all disturbances with wavelengths greater than $\lambda_c$ are unstable. Thus, any factor decreasing $\lambda_c$ will help to destabilize the interface.

Before applying the knowledge gained from film boiling to electrostatic suppression of the Leidenfrost state, two particular issues must be considered. First, unlike in film boiling where the liquid-vapor interface eventually ruptures and the vapor phase is discharged as rising bubbles into the bulk liquid, vapor travels in the gap space between the Leidenfrost drop and the substrate and escape to the ambient from the outer edge of the drop. Hence, the transverse dimensions of the liquid-vapor interface are restricted by the drop's apparent contact length on the substrate ($\xi = 2a$). Since only disturbances having wavelengths greater than $\lambda_c$ can grow, the transverse extent of the interface has a critical impact on the instability, for instance, if $\xi$ happens to be less than $\lambda_c$, all disturbances will be quickly damped. Second, Eq. (36) was derived for Rayleigh-Taylor instability, where both the liquid phase and the vapor phase are treated as stationary, but the relative motion between the two phases is non-negligible in the Leidenfrost drop. To obtain an accurate estimate of $\lambda_c$, a revised dispersion relationship will be developed by considering the Kelvin-Helmholtz instability with the phasic velocity difference.

As illustrated in Fig. 5 the liquid-vapor interface of the Leidenfrost drop is assumed to be an originally flat horizontal plane located at $z = 0$. The liquid and vapor phases are moving with $\bar{u}_l$ and $\bar{u}_v$, respectively, parallel to the undisturbed interface. The Kelvin-Helmholtz instability analysis can be performed following the framework outlined in [58] and the details will not be presented here. Accordingly, the new dispersion equation is derived as

$$s^2 = \frac{\sigma_{lv}}{\rho_l + \rho_v}k^3 - \frac{(\rho_l - \rho_v)g}{\rho_l + \rho_v}k - \frac{f(E, \varepsilon_l, \varepsilon_v)}{\rho_l + \rho_v}k^2\coth(k\delta)$$
$$- \frac{\rho_l\rho_v}{(\rho_l + \rho_v)^2}(\bar{u}_v - \bar{u}_l)^2k^2 \quad (38)$$

Comparing to Eq. (36), the phasic velocity difference ($\bar{u}_v - \bar{u}_l$) will further destabilize the interface by promoting long-wavelength disturbances. Since $\bar{u}_l \ll \bar{u}_v$, the liquid velocity $\bar{u}_l$ is usually discarded and the velocity difference can be simplified to $\bar{u}_v - \bar{u}_l \approx \bar{u}_v = u_m$. Moreover, considering the fact that $\coth(k\delta) \approx \frac{1}{k\delta}$ for $k\delta << 1$, the final form of the dispersion relation for electrohydrodynamic instability pertinent to a Leidenfrost drop becomes
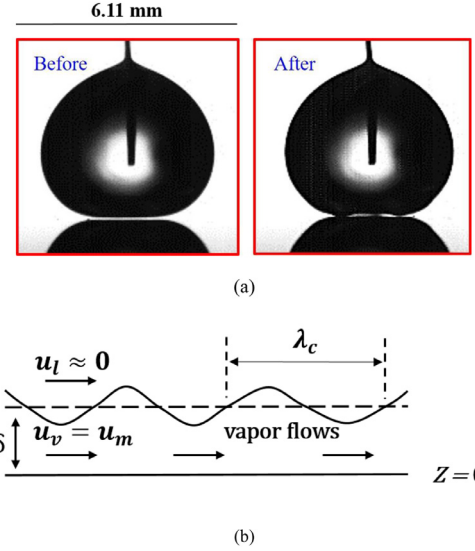


**Fig. 5.** (a) Profiles of the vapor layer of a Leidenfrost drop before and after the electric field is applied; and (b) Schematic of interfacial instability.

$$s^2 = \frac{\sigma_{lv}}{\rho_l + \rho_v}k^3 - \frac{(\rho_l - \rho_v)g}{\rho_l + \rho_v}k - \frac{f(E, \varepsilon_l, \varepsilon_v)}{\rho_l + \rho_v}\frac{k}{\delta} - \frac{\rho_l\rho_v u_m^2}{(\rho_l + \rho_v)^2}k^2 \quad (39)$$

The critical wavenumber and wavelength, $k_c$ and $\lambda_c$, are calculated from Eq. (39)

$$k_c = \frac{\left(\frac{\rho_l\rho_v u_m^2}{\rho_l + \rho_v}\right) + \sqrt{\left(\frac{\rho_l\rho_v u_m^2}{\rho_l + \rho_v}\right)^2 + 3\sigma_{lv}\left[g(\rho_l - \rho_v) + \frac{f}{\delta}\right]}}{3\sigma_{lv}} \quad (40)$$

$$\lambda_c = 2\pi\frac{-\left(\frac{\rho_l\rho_v u_m^2}{\rho_l + \rho_v}\right) + \sqrt{\left(\frac{\rho_l\rho_v u_m^2}{\rho_l + \rho_v}\right)^2 + 3\sigma_{lv}\left[g(\rho_l - \rho_v) + \frac{f}{\delta}\right]}}{\left[g(\rho_l - \rho_v) + \frac{f}{\delta}\right]} \quad (41)$$

where the parameters, $u_m, \delta$ and $f$, can be solved from the foregoing force balance model. It is easy to see that if the effects of the phasic velocity difference and electric field are absent, Eqs. (40) and (41) will reduce to the classical results in [79]. Indeed, both factors increase $k_c$ (equivalently, decrease $\lambda_c$), thereby promoting instability at the interface. In the above analysis, the effects of viscosity and evaporation on stability are not expressed explicitly, but rather, they are embodied through the vapor velocity $u_m$ and the vapor layer thickness $\delta$.

Once $\lambda_c$ is calculated from Eq. (41), it can be compared with the contact length of the Leidenfrost drop $\xi$ to determine the interfacial stability. If $\lambda_c > \xi$, no disturbance with wavelength $\lambda > \lambda_c$ is physically possible and the interface will be stable. Otherwise, the interface will be destabilized causing the Leidenfrost state to vanish. Hence, the instability criterion can be set as

$$\lambda_c \leq \xi \quad (42)$$

Since $u_m$ and $\delta$ in Eq. (41) depend on the wall superheat $\Delta T$, the LFP can be predicted from the instability criterion for given drop size and electric field conditions, i.e., a Leidenfrost drop is stable only if $\Delta T$ is sufficiently high such that $\lambda_c > \xi$ can be satisfied. Reversely, since the term $f$ in Eq. (41) is dictated by the electric field, the amplitude and frequency of the electric field necessary for suppressing the Leidenfrost state can be deduced from the instability criterion for given drop size and wall superheat.
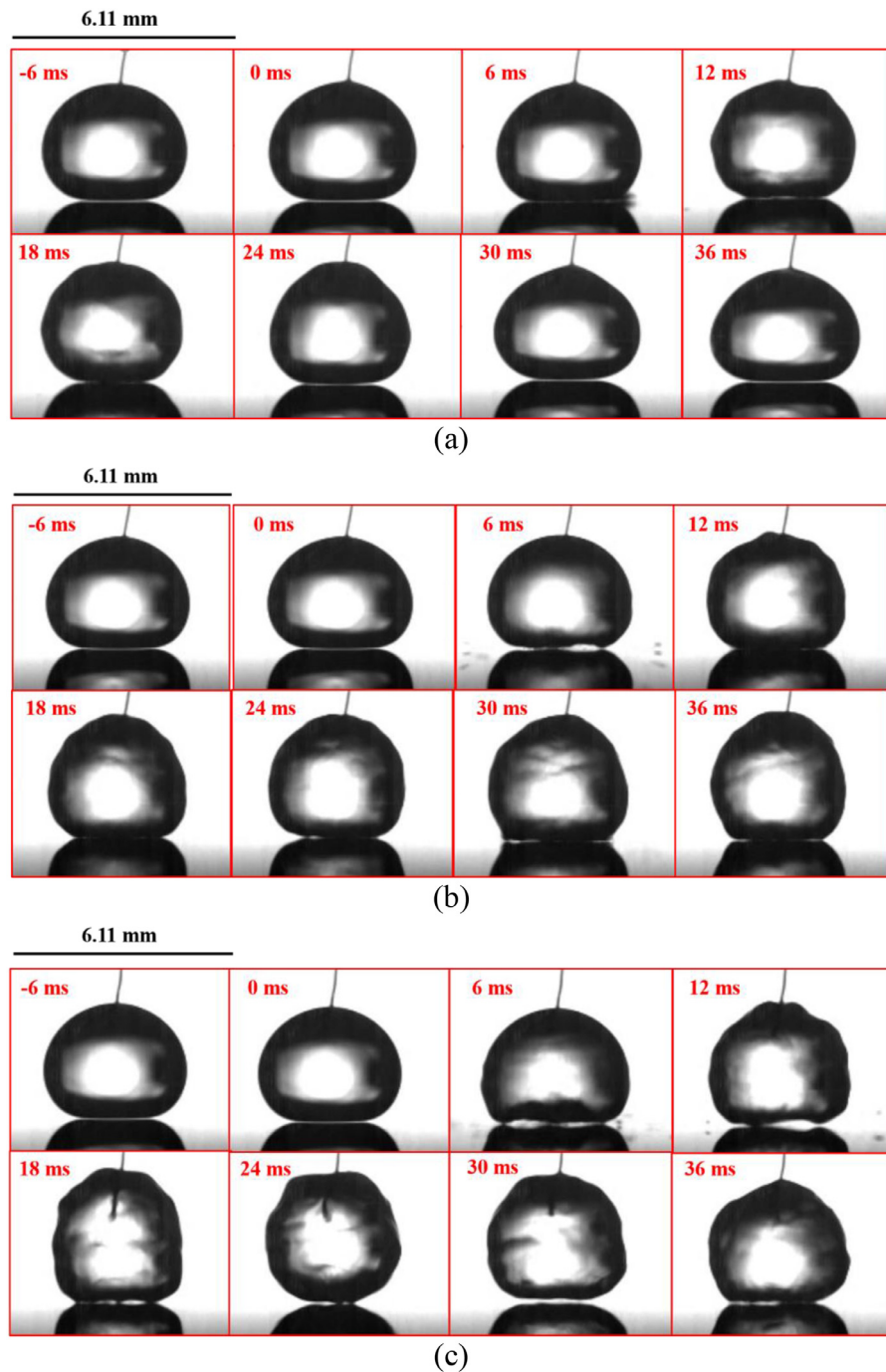
**Fig. 6.** Dynamics of a Leidenfrost drops under the influence of DC fields: (a) $V = 56$ V; (b) $V = 100$ V and (c) $V = 140$ V (Wall temperature $T_w = 200$ °C).

## 4. Results and discussion

### 4.1. Dynamics of Leidenfrost drop under electric fields

A high-speed optical camera and an infrared camera were synchronized to observe the electrostatic suppression process. The experimental results presented in the following are for a water drop with an initial volume of 20 μL. In the experiments, the average wall temperature was set at $T_w = 200$°C.

Fig. 6 depicts the time series of the instantaneous morphology of a Leidenfrost drop when subject to DC voltages of 56 V, 100 V and 140 V, respectively. In all three cases, the electric signal is turned on at $t = 0$ ms. Before that ($t = -6$ ms), the drop is

undergoing the Leidenfrost state, evidenced by the existence of a stable vapor cushion (shown as a gap between the drop and its mirror image reflected from below). After a 56 V voltage is applied (Fig. 6(a)), the drop is pulled downward by the electrostatic attraction force to touch the superheated substrate ($t = 6$ ms). The abrupt solid-liquid contact leads to immense vapor generation that perturbs and even ruptures the liquid-vapor interface with tiny satellite droplets splashing out from the edge (Note: this can be better observed at the same time instant, $t = 6$ ms, in Fig. 6(b) and (c)). The disturbance waves grow and propagate along the drop surface, causing the drop to deform slightly from the original truncated spherical shape ($t = 12$ ms). However, since the electric field is not strong enough and the drop is also losing mass
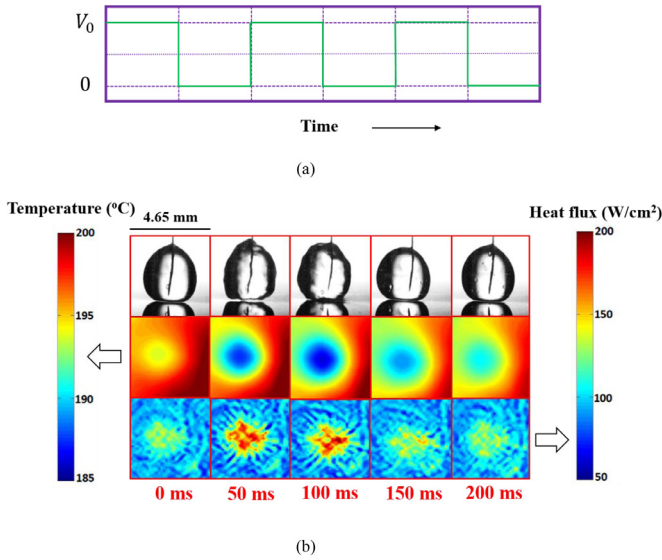
**Fig. 7.** (a) Waveform of the square pulse wave signal used for electrostatic suppression of the Leidenfrost state; and (b) Optical observation and measurements of the wall temperature and heat flux for a Leidenfrost drop ($V_0 = 80$ V and $T_w = 200°$C).

**Fig. 8.** Evaporation time of a water droplet at different conditions, where the LFP for each case is marked by an arrow (The error bars in the $t_e$ measurement are too small to be shown).

due to evaporation and droplet ejection, the viscous pressure of the vapor flow soon overruns the sum of the electric and gravitational forces. As a result, the direct solid-liquid contact is short lived and the disturbance waves decay very rapidly ($t = 24$ ms). At $t = 30$ ms, the drop restores to its stable Leidenfrost configuration. When a higher voltage ($V = 100$ V) is actuated, the electrostatic force increases nearly four times. This helps draw the Leidenfrost drop to closer vicinity of the wall, as indicated in Fig. 6(b), but is still insufficient to subdue the viscous pressure. At the new "equilibrium" ($t = 36$ ms), the image suggests that a vapor layer, although visually much thinner than that in Fig. 6(a), exists between the drop and the substrate. Through this miniscule gap, fast vapor flow stimulates interfacial oscillations that spread over the entire surface of the drop, resulting in a drop shape quite different from a standard Leidenfrost drop. If the applied voltage is further increased to $V = 140$ V, the drop becomes unstable. As shown in Fig. 6(c), the liquid-vapor interface is severely distorted and, instead of floating over a vapor layer, the drop is connected to the substrate by multiple liquid filaments extruding from its bottom. The static images may leave that impression that the solid-liquid contact is only sporadic and intermittent, but, in fact, liquid fingering occurs with such a high frequency that the substrate is rewetted at multiple spots at any time instant. This is because the strong effects of the electric force and the phasic velocity difference always destabilize the interface.

Fig. 7 illustrates a sample result of the Leidenfrost state suppression using a square pulse wave signal. To compare with the DC cases, a 50% duty cycle square pulse wave with an amplitude of 80 V and an actuation duration of 100 ms per period was used. The waveform is shown schematically in Fig. 7(a). The initial drop size and wall temperature are identical to those in Fig. 6. The optical images in the first row of Fig. 7(b) show the shape variation of the drop during one signal cycle. When the voltage is suddenly turned on ($t = 0 \sim 100$ ms), the drop behavior resembles that under the DC field, characterized by an oscillating interface and liquid filaments extruding toward the solid surface. When the voltage is turned off ($t = 100 \sim 200$ ms), the drop is able to resume a stable Leidenfrost state. The images in the second row of Fig. 7(b) illustrate the temperature signature of the drop on the solid surface obtained from the IR temperature measurements. At $t = 0$ ms, even though there is no solid-liquid contact, the area right
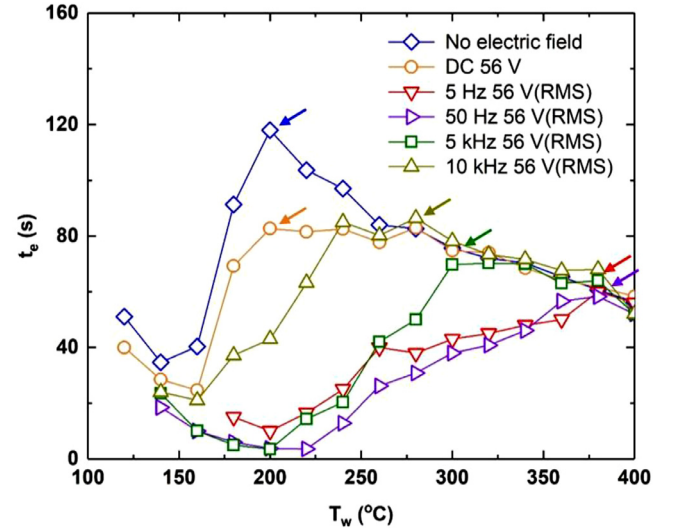
beneath the drop (i.e., the apparent contact area of the drop) exhibits a lower temperature than the neighboring area due to cooling from the flow of evaporated vapor. Once the liquid-solid contacts are initiated by the electrostatic suppression mechanism, the temperature of the same region decreases drastically owing to the transient conduction through the liquid, as indicated by the deep blue color. The local temperature reaches its minimum at the end of the active 50% duty cycle ($t = 100$ ms). When the electric force vanishes afterwards, the surface temperature goes up gradually as the suppressed drop returns to the Leidenfrost state. The corresponding heat flux distributions are computed from the temperature data and the results are depicted in the third row of Fig. 7(b). Clearly, the high-flux regions (shown in bright colors) can be correlated with the cold spots in the temperature map. While there is no intention to quantify heat transfer associated with the Leidenfrost drop in this work, it is worth noting that the maximum heat flux reaches 150 – 200 W/cm$^2$ at the solid-liquid contact recreated by the electrostatic suppression.

### 4.2. Experimental determination of LFP

Six sets of experiments were conducted to measure the evaporation time of a 20 μL water drop, $t_e$, as a function of the wall surface temperature, $T_w$. These include one baseline experiment without the electric field, one with a DC field and four with AC fields of different driving frequencies. In each experiment, $T_w$ was varied between 100 °C and 400 °C with a 20 °C increment. The measured data are shown in Fig. 8, where the Leidenfrost point, $T_{LFP}$, is determined as $T_w$ corresponding to the longest evaporation time (marked by a colored arrow for each experimental condition). The baseline experiment yields $T_{LFP} = 200°$C. When a DC voltage of $V = 56$ V is applied, no improvement in LFP is observed, because the electric field is insufficient to suppress the Leidenfrost state. When AC signals with $V_{RMS} = 56$ V are applied, the LFP is enhanced in general. The data also indicates a frequency dependence. The greatest improvement is found at low frequencies, e.g., $T_{LFP}$ surges to 380 °C at $f_E = 5$ Hz and remains largely unchanged till $f_E = 50$ Hz. Then the LFP enhancement deteriorates at much higher frequencies, e.g., $T_{LFP}$ decreases to 300°C at $f_E = 5$ kHz and 260°C at $f_E = 10$ kHz. The threshold voltage for DC-suppression and the frequency-dependent LFP enhancement for AC-suppression will be discussed in the following sections.
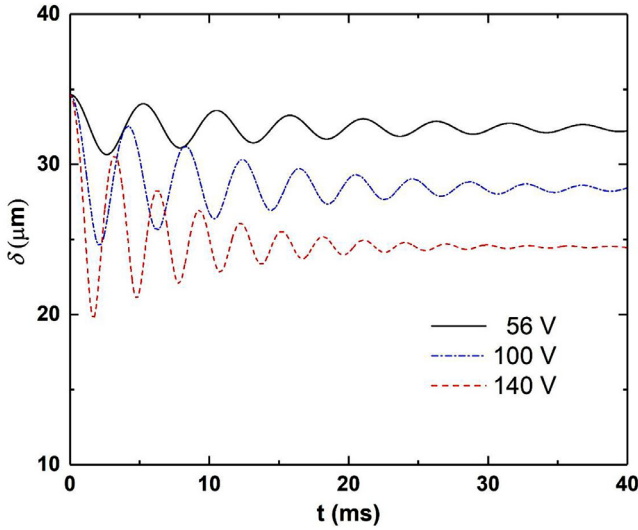
**Fig. 9.** Variation of the vapor layer thickness $\delta$ for different DC fields (V = 56 V, 100 V and 140 V) at $T_w = 300\,°C$.



**Fig. 10.** Variation of the vapor layer thickness $\delta$ for different AC fields ($f_E = 5$ Hz, 50 Hz and 5 kHz) at $V_{RMS} = 56$ V and $T_w = 300\,°C$.

### 4.3. Prediction of vapor layer thickness

The vapor layer thickness $\delta$ plays a crucial role in the stability of a Leidenfrost drop. According to the foregoing theoretical analysis, it determines the strength of the electric field, the evaporation rate, the viscous pressure and the phasic velocity difference. By solving Eq. (32) with two initial conditions, the time history of $\delta$ can be obtained for both DC and AC electric fields.

Fig. 9 shows the variation of $\delta$ for a Leidenfrost drop residing on a hot surface of $T_w = 300^oC$ when exposed to DC fields. Overall, the liquid-vapor interface of the drop falls from its initial position at $\delta_0 = 34.6\ \mu$m and undergoes a few cycles of damped oscillations before reaching a new steady state position. The process resembles the response of an underdamped harmonic oscillator to a step stimulus, except that the restoring and damping mechanisms are due primarily to the interplay of the viscous pressure and the electric force, both being nonlinear with respect to the displacement from the original position. Owing to the complexity of Eq. (32), it is infeasible to deduce analytically the natural frequencies of the oscillating Leidenfrost drop. Since the final equilibrium position is determined by the balance of various forces, the highest voltage corresponding to the greatest electric force (V = 140 V) yields the least $\delta$.

When an AC field is applied, the motion of the interface, governed by Eq. (32), mimics a harmonic oscillator stimulated by a sinusoidal driving force, as depicted in Fig. 10. It is further observed that the temporal response of the system is strongly affected by the frequency of the AC field. At the lowest frequency, $f_E = 5$ Hz, the variation of $\delta$ initially exhibits some irregular oscillations, due to inertia, and then follows the external field. The quasi-steady oscillations proceed with a doubled frequency ~ 10 Hz since the electric force scales as the square of the applied field $F_e \sim E^2$ (indicated by Eq. (31)). When $f_E$ increases to 50Hz , after some initial fluctuations, $\delta$ oscillates with a frequency ~ 100 Hz and an amplitude slightly greater than that at 5 Hz. At a much higher driving frequency, $f_E = 5$ kHz, the drop still undulates but the oscillation quickly dampens out. Here it is very tempting to correlate the oscillating behavior of the interface to the drop's resonant frequencies, which can be estimated by $f_n = \sqrt{\frac{n(n-1)(n+2)\sigma_{lv}}{4\pi^2 \rho_l R^3}}$ (where $n$ is the number of nodes in the oscillation) [81,82], especially, $f_2 \approx 51$ Hz. However, $f_n$ is derived for resonant vibrations of the free surface of a drop, which are driven by the periodic conversion be-
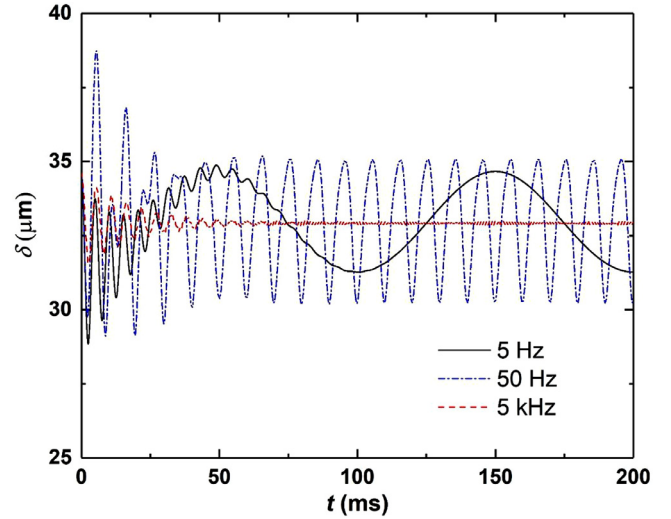
tween kinetic energy and surface energy, and is thus not directly relevant to the interface motion considered in this work.

Nevertheless, the most significant finding from Fig. 10 is that the computed values of $\delta$ never reduce to zero although the Leidenfrost state is shown to be suppressed at $f_E = 5$ Hz and 50 Hz (refer to the experimental results in Fig. 8). This is a natural consequence of the force balance model arising from the dominant role of the viscous pressure force at the small $\delta$ limit. Hence, the force balance argument alone cannot fully resolve the mechanisms of the Leidenfrost state suppression by electric field.

### 4.4. Kelvin-Helmholtz instability

Once the vapor layer thickness $\delta$ is calculated, the mean vapor velocity $u_m$ and the critical wavelength of the interfacial disturbances $\lambda_c$ can be found from Eqs. (13) and (41), respectively. Fig. 11(a) shows the temporal variations of $\delta$, $u_m$ and $\lambda_c$ for a Leidenfrost drop under a DC voltage V = 56 V at a prescribed wall temperature $T_w = 300$ °C. It is observed that $\delta$ and $u_m$ are out of phase with each other, whereas $\delta$ and $\lambda_c$ evolve in phase. Whenever $\delta$ diminishes, the vapor flow is accelerated due to both the greater evaporation and the smaller flow area available for the vapor to escape. In the meanwhile, the electric field across the vapor layer becomes stronger. These factors together lead to a decrease in $\lambda_c$, making the liquid-vapor interface more vulnerable to instabilities. It is important to note that while $\lambda_c$ fluctuates over time, it is the minimum of the instantaneous values, $\lambda_{c,min}$, that determines the interfacial stability. Fig. 11(a) shows that $\lambda_{c,min} = 2.4$ mm, corresponding to $\delta_{min} = 31\ \mu$m and $u_{m,max} = 2$ m/s, is greater than $\xi = 2a = 2.2$ mm. Thus, the interfacial disturbances will decay and the Leidenfrost state persists. In contrast, Fig. 11(b) illustrates that at higher voltages, $\lambda_{c,min}$ may decrease below $\xi$, for instance, $\lambda_{c,min} = 0.9$ mm at 100 V and $\lambda_{c,min} = 0.5$ mm at 140 V, and the Leidenfrost drop will be destabilized in both cases.

Fig. 12 shows the evolutions of $\delta$, $u_m$ and $\lambda_c$ of a Leidenfrost drop exposed to AC electric fields. Three different driving frequencies are considered, $f_E = 5$ Hz, 50 Hz and 5 kHz, while the RMS voltage remains a constant $V_{RMS} = 56$ V. The wall temperature is set at $T_w = 300$ °C. The waveform of the sinusoidal AC signal is included in the figure to facilitate the discussion. Compared to the DC results, the instantaneous growth of $\lambda_c$ cannot be correlated with $\delta$ and $u_m$ in a simple manner, but the minimum value $\lambda_{c,min}$ does appear concomitantly at $\delta_{min}$ and $u_{m,max}$ when the voltage
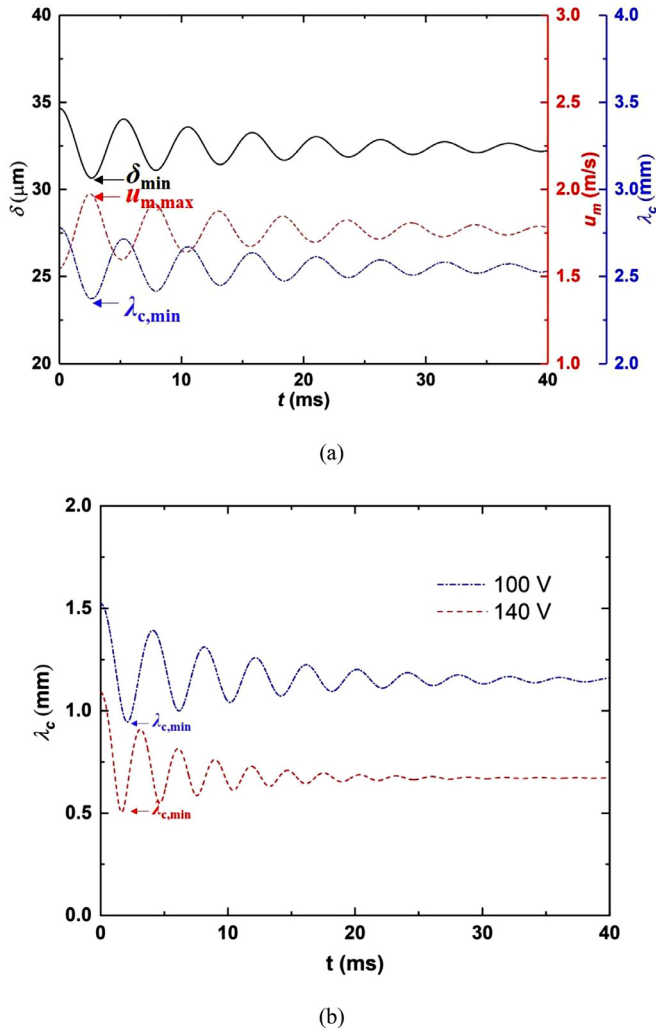
(a)



(b)

**Fig. 11.** (a) Variation of the vapor layer thickness $\delta$, vapor velocity $u_m$ and critical wavelength $\lambda_c$ of the interface after a DC signal ($V = 56$ V) is applied; and (b) Variation of the critical wavelength after DC signals ($V = 100$ V and 140 V) are applied ($T_w = 300$ °C).



(a)



(b)



(c)

**Fig. 12.** Variation of the vapor layer thickness $\delta$, vapor velocity $u_m$ and critical wavelength $\lambda_c$ of the interface after AC signals ((a) $f_E = 5$ Hz, (b) 50 Hz and (c) 5 kHz) are applied ($V_{RMS} = 56$ V and $T_w = 300$ °C).

reaches its peak. For the given $V_{RMS}$ and $T_w$, $\lambda_{c,min}$ is determined to be 1.9 mm, 1.9 mm and 2.2 mm for $f_E = 5$ Hz, 50 Hz, and 5 kHz, respectively. According to the instability criterion $\lambda_{c,min} \leq \xi$ and $\xi = 2.2$ mm, it is deduced that the Leidenfrost drop will be suppressed by AC signals at 5 Hz and 50 Hz but not at 5 kHz, which is consistent with the experimental results in Fig. 8.

The dependence of $\lambda_{c,min}$ on the electric field is further illustrated in Fig. 13, where $\lambda_{c,min}$ is plotted in the parameter space defined by $V_{RMS}$ and $f_E$ at a wall temperature of 300 °C. Two general trends can be detected: 1) $\lambda_{c,min}$ decreases with increasing $V_{RMS}$, i.e., higher voltage tends to destabilize the Leidenfrost state; and 2) $\lambda_{c,min}$ is not very sensitive to $f_E$ at the low frequency range but quickly increases for higher frequencies, i.e., electrostatic suppression of the Leidenfrost state is more effective at low frequencies. Imposing $\xi$ (the apparent contact length of the drop) as the gray-colored plane in Fig. 13(a), the parameter space will be demarcated into an upper "stable" region, where $\lambda_{c,min} > \xi$ and the Leidenfrost drop will survive, and a lower "unstable" region, where $\lambda_{c,min} \leq \xi$ and the Leidenfrost state is suppressed. To observe this better, the isolines of $\lambda_{c,min}$ are plotted in Fig. 13(b) with $f_E$ and $V_{RMS}$ as the coordinates. Clearly, at a prescribed wall temperature, the unstable region is bounded by the envelope $\lambda_{c,min} = \xi$. It is only attainable within a certain voltage-frequency range, that is, the voltage must
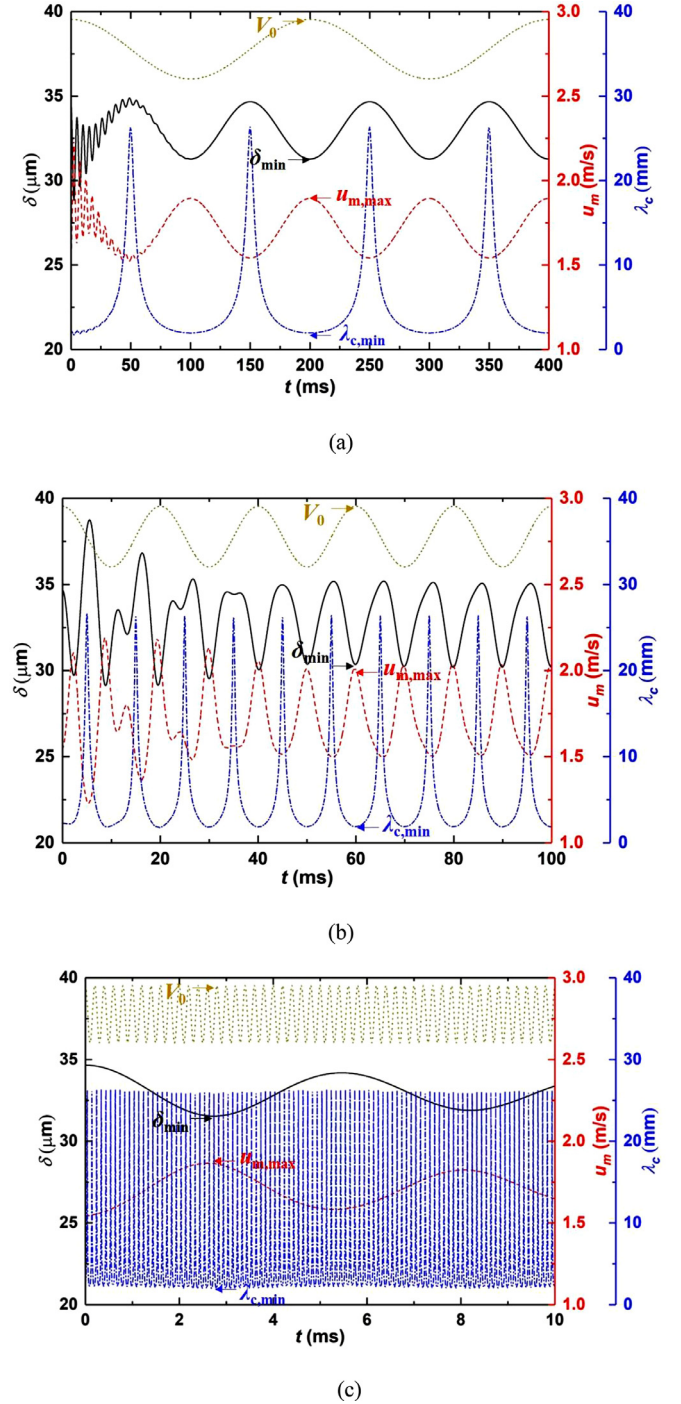
be sufficiently high and the frequency must be sufficiently low to suppress the Leidenfrost state. Within this region, the LFP can be enhanced to a higher value by tuning the voltage and frequency of the AC field. Additionally, upticks are observed at about $f_E = 100$ Hz in Fig. 13(b), implying that a lower voltage is required to reach $\lambda_{c,min}$. This is supposed to be related to the natural frequency of the interface motion at which the maximum oscillation of $\delta$ takes place. Unfortunately, a straightforward estimate of this natural frequency is prohibited by the complex form of Eq. (32) and will be addressed in future study.
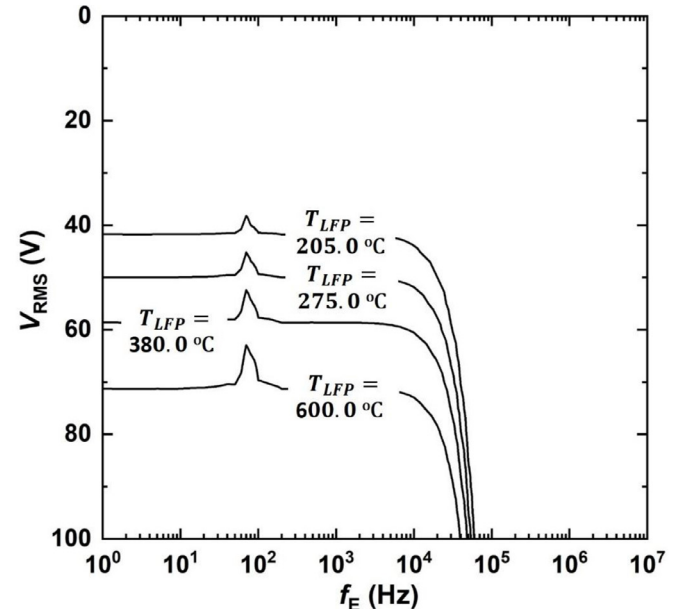
(a)



(a)
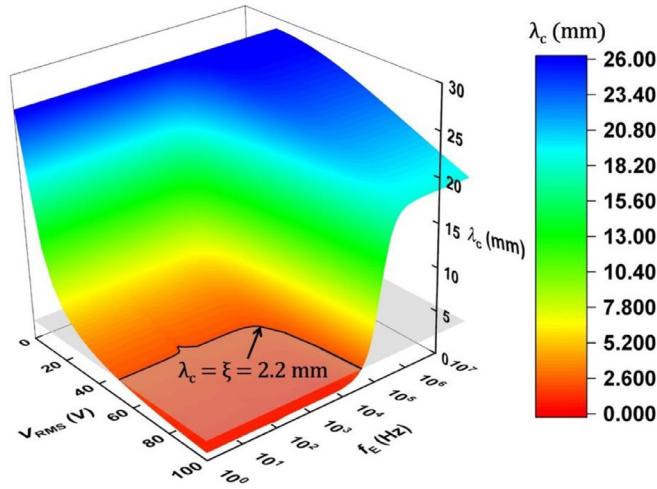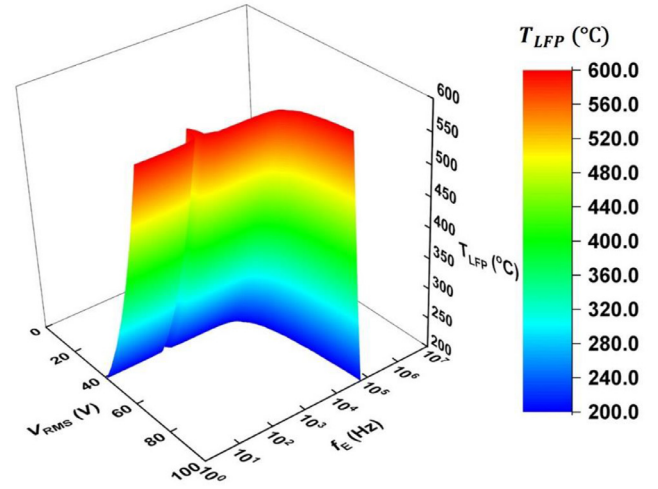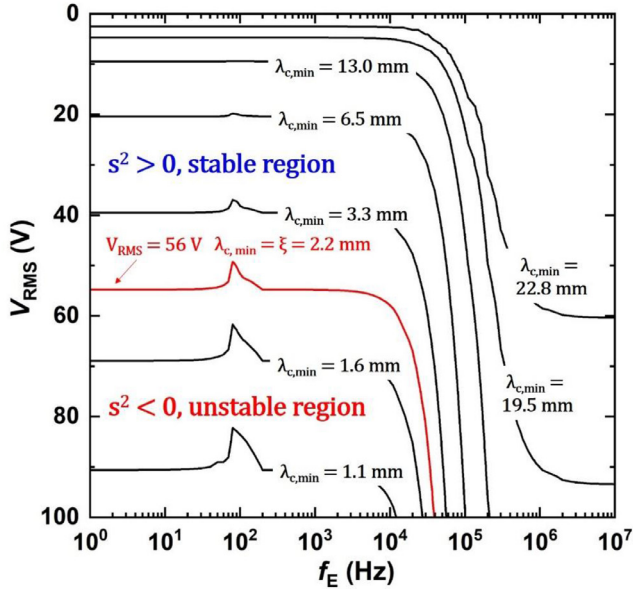


(b)

**Fig. 13.** Dependence of the minimum critical wavelength $\lambda_{c,min}$ on the electric field at prescribed wall temperature $T_w = 300°C$.



(b)

**Fig. 14.** Dependence of the LFP on the electric field.

### 4.5. Leidenfrost temperature

In the foregoing analysis, $\lambda_{c,min}$ is determined as a function of $f_E$ and $V_{RMS}$ for a prescribed wall temperature and the Leidenfrost state corresponds to the criterion $\lambda_{c,min} = \xi$. Since $\lambda_{c,min}$ also depends on the wall superheat, the LFP can be deduced reversely for given electric field conditions, as shown in Fig. 14, which allows the LFP to be determined for any combination of $V_{RMS}$ and $f_E$. The LFP isolines in Fig. 14(b) indicate that, compared to the baseline case without electric field $T_{LFP} = 200°C$, the LFP is enhanced to 205°C when an AC voltage signal of $V_{RMS} = 42$ V is applied over a wide range of frequencies (in fact, a lower voltage is needed around 100 Hz, probably due to the resonant behavior of the interface). As the driving frequency goes beyond 4 kHz (i.e., the charge relaxation frequency for water [83]), the conducting liquid starts to behave like a dielectric and the electric field no longer concentrates across the vapor layer. Hence, much higher voltages are re-

quired to sustain the electrostatic suppression mechanism. Similar trends can be found from the other isolines. Lastly, the theoretical predictions of LFP are compared in Fig. 15 with the experimental results for a fixed voltage $V_{RMS} = 56$ V. The reasonable agreement suggests that the analytical model developed in this work captures the key physics of the electrostatic suppression and can be used as a design tool to predict the LFP in relevant phase change heat transfer applications.

### 5. Conclusions

Electrostatic suppression of the Leidenfrost state was studied both experimentally and theoretically with the aim to address some critical drawbacks in the current understanding of the suppression mechanisms. The dynamics of a Leidenfrost drop was visualized and the Leidenfrost temperature was determined under the influence of both DC and AC electric fields. An analytical model was formulated to identify the physical origin of the Leidenfrost suppression and to determine the Leidenfrost temperature for
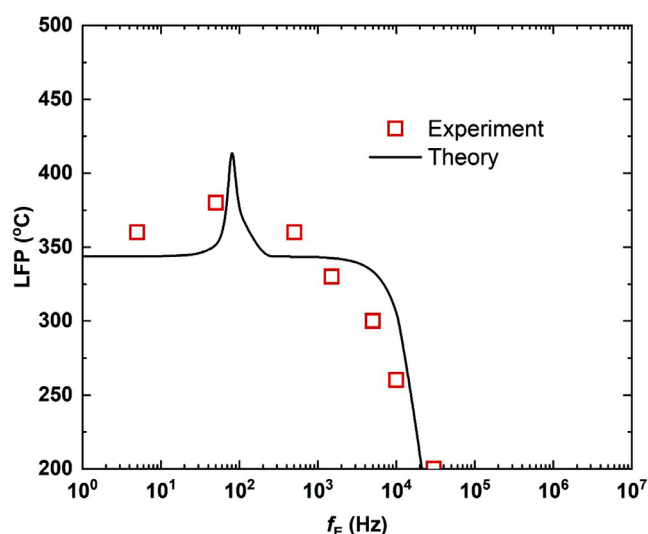
**Fig. 15.** Comparison of the experimental measurements and the theoretical predictions of the LFP at different frequencies for a prescribed voltage $V_{RMS} = 56$ V.

given fluid type and applied electrical signal, which may be employed as a predictive tool for practical design of heat transfer devices involving the Leidenfrost phenomenon. The key findings are summarized below.

1. The Leidenfrost state can be effectively suppressed by applying a DC or AC electric field and the LFP is greatly enhanced. For DC suppression, the degree of LFP enhancement is proportional to the voltage. For AC suppression, the maximum LFP enhancement occurs near the natural frequency associated with the interfacial motion, but starts to fade when the driving frequency passes the charge relaxation frequency of the liquid.

2. The existing force balance models and linear instability analysis are found inadequate in revealing the full mechanisms of Leidenfrost suppression. The former group requires some arbitrary threshold vapor layer thickness to assert a successful suppression, whereas the latter is limited largely to the analysis of conducting liquids in DC field and does not yield a direct prediction of the LFP.

3. A new theoretical approach was developed in this work which first derives the vapor layer dynamics from the force balance argument and then applies the Kelvin-Helmholtz instability analysis to determine an interfacial instability criterion. This model is able to predict directly the LFP for given electric field conditions as well as the electric field needed to suppress the Leidenfrost state at prescribed wall temperature. Moreover, this model is applicable to both conduction and dielectric fluids enhanced by either DC or AC field.

## Declaration of Competing Interest

The authors declare that they have no known competing financial interests or personal relationships that could have appeared to influence the work reported in this paper.

## CRediT authorship contribution statement

**Yi Lu:** Conceptualization, Data curation, Formal analysis, Investigation, Software, Validation, Visualization, Writing - original draft, Writing - review & editing. **Jiming Bao:** Resources, Investigation. **Dong Liu:** Conceptualization, Formal analysis, Funding acquisition, Investigation, Methodology, Project administration, Resources, Supervision, Writing - original draft, Writing - review & editing.

## References

[1] R.H. Chen, L.C. Chow, J.E. Navedo, Effects of spray characteristics on critical heat flux in subcooled water spray cooling, Int. J. Heat Mass Transf. 45 (19) (2002) 4033–4043.

[2] Y. Zhang, M. Jia, H. Liu, M. Xie, T. Wang, Investigation of the characteristics of fuel adhesion formed by spray/wall interaction under diesel premixed charge compression ignition, At. Sprays. 25 (11) (2015) 933–968.

[3] D.D. Hall, I. Mudawar, R.E. Morgan, S.L. Ehlers, Validation of a systematic approach to modeling spray quenching of aluminum alloy extrusions, composites, and continuous castings, J. Mater. Eng. Perform. 6 (1) (1997) 77–92.

[4] G. Liang, I. Mudawar, Review of spray cooling - part 2: high temperature boiling regimes and quenching applications, Int. J. Heat Mass Transf. 115 (2017) 1206–1222.

[5] A. Chausalkar, C.B.M. Kweon, S.C. Kong, J.B. Michael, Leidenfrost behavior in drop-wall impacts at combustor-relevant ambient pressures, Int. J. Heat Mass Transf. 153 (2020) 9.

[6] P.F. Fu, L.Y. Hou, Z.Y. Ren, Z. Zhang, X.F. Mao, Y.S. Yu, A droplet/wall impact model and simulation of a bipropellant rocket engine, Aerosp. Sci. Technol. 88 (2019) 32–39.

[7] J.G. Wang, X.Y. Huang, X.Q. Qiao, D.H. Ju, C.H. Sun, Experimental study on effect of support fiber on fuel droplet vaporization at high temperatures, Fuel 268 (2020) 9.

[8] B.S. Gottfried, K.J. Bell, Film boiling of spheroidal droplets. Leidenfrost phenomenon, Ind. Eng. Chem. Fundam. 5 (4) (1966) 561–568.

[9] J.D. Bernardin, I. Mudawar, The Leidenfrost point: Experimental study and assessment of existing models, J. Heat Transf. 121 (4) (1999) 894–903.

[10] J.M. Ramilison, J.H. Lienhard, Transition boiling heat transfer and the film transition regime, transactions of the ASME, J. Heat Transf. 109 (3) (1987) 746–752.

[11] V.K. Dhir, S.P. Liaw, Framework for a unified model for nucleate and transition pool boiling, transactions of the ASME, J. Heat Transf. 111 (3) (1989) 739–747.

[12] R.L. Johnson, Effect of an electric field on boiling heat transfer, AIAA J. 6 (8) (1968) 1456–1460.

[13] G.S. Emmerson, The effect of pressure and surface material on the leidenfrost point of discrete drops of water, Int. J. Heat Mass Transf. 18 (3) (1975) 381–386.

[14] S.G. Kandlikar, M.E. Steinke, Contact angles and interface behavior during rapid evaporation of liquid on a heated surface, Int. J. Heat Mass Transf. 45 (18) (2002) 3771–3780.

[15] Y. Takata, S. Hidaka, J.M. Cao, T. Nakamura, H. Yamamoto, M. Masuda, T. Ito, Effect of surface wettability on boiling and evaporation, Energy 30 (2–4) (2005) 209–220.

[16] I.U. Vakarelski, N.A. Patankar, J.O. Marston, D.Y.C. Chan, S.T. Thoroddsen, Stabilization of Leidenfrost vapour layer by textured superhydrophobic surfaces, Nature 489 (7415) (2012) 274–277.

[17] T.Y. Zhao, N.A. Patankar, The thermo-wetting instability driving Leidenfrost film collapse, PNAS 117 (24) (2020) 13321–13328.

[18] L. Zhong, Z. Guo, Effect of surface topography and wettability on the Leidenfrost effect, Nanoscale 9 (19) (2017) 6219–6236.

[19] V. Talari, P. Behar, Y. Lu, E. Haryadi, D. Liu, Leidenfrost drops on micro/nanostructured surfaces, Front. Energy 12 (1) (2018) 1–21.

[20] S.H. Kim, G. Lee, H. Kim, M.H. Kim, Leidenfrost point and droplet dynamics on heated micropillar array surface, Int. J. Heat Mass Transf. 139 (2019) 1–9.

[21] T. Tran, H.J.J. Staat, A. Susarrey-Arce, T.C. Foertsch, A. van Houselt, H. Gardeniers, A. Prosperetti, D. Lohse, C. Sun, Droplet impact on superheated micro-structured surfaces, Soft Matter 9 (12) (2013) 3272–3282.

[22] I.W. Park, M. Fernandino, C.A. Dorao, Effect of micropillar characteristics on Leidenfrost temperature of impacting droplets. ASME 2016 14th International Conference on Nanochannels, Microchannels, and Minichannels, ICNMM2016-7963, Washington, DC, USA.

[23] D.A. del Cerro, A.G. Marin, G. Romer, B. Pathiraj, D. Lohse, A.J.H. in't Veld, Leidenfrost point reduction on micropatterned metallic surfaces, Langmuir 28 (42) (2012) 15106–15110.

[24] H. Nair, H.J.J. Staat, T. Tran, A. van Houselt, A. Prosperetti, D. Lohse, C. Sun, The Leidenfrost temperature increase for impacting droplets on carbon-nanofiber surfaces, Soft Matter 10 (13) (2014) 2102–2109.

[25] R. Hays, D. Maynes, J. Crockett, Thermal transport to droplets on heated superhydrophobic substrates, Int. J. Heat Mass Transf. 98 (2016) 70–80.

[26] W.S. Bradfield, Liquid-solid contact in stable film boiling, Ind. Eng. Chem. Fundam. 5 (2) (1966) 200–204.

[27] H. Kim, J. Buongiorno, L.-W. Hu, T. McKrell, Nanoparticle deposition effects on the minimum heat flux point and quench front speed during quenching in water-based alumina nanofluids, Int. J. Heat Mass Transf. 53 (7) (2010) 1542–1553.

[28] S. Sinha-Ray, Y. Zhang, A.L. Yarin, Thorny devil nanotextured fibers: the way to cooling rates on the order of 1 kW/cm2, Langmuir 27 (1) (2010) 215–226.

[29] C.M. Weickgenannt, Y. Zhang, S. Sinha-Ray, I.V. Roisman, T. Gambaryan-Roisman, C. Tropea, A.L. Yarin, Inverse-Leidenfrost phenomenon on nanofiber mats on hot surfaces, Phys. Rev. E 84 (3) (2011) 036310.

[30] C.M. Weickgenannt, Y. Zhang, A.N. Lembach, I.V. Roisman, T. Gambaryan-Roisman, A.L. Yarin, C. Tropea, Nonisothermal drop impact and evaporation on polymer nanofiber mats, Phys. Rev. E 83 (3) (2011) 036305.

[31] S.H. Kim, H.S. Ahn, J. Kim, M. Kaviany, M.H. Kim, Dynamics of water droplet on a heated nanotubes surface,, Appl. Phys. Lett. 102 (23) (2013) 233901.

[32] R.L. Agapov, J.B. Boreyko, D.P. Briggs, B.R. Srijanto, S.T. Retterer, C.P. Collier, N.V. Lavrik, Asymmetric wettability of nanostructures directs Leidenfrost droplets, ACS Nano 8 (1) (2013) 860–867.

[33] M. Auliano, M. Fernandino, P. Zhang, C.A. Dorao, The Leidenfrost phenomenon on silicon nanowires, ASME 2016 14th International Conference on Nanochannels, Microchannels, and Minichannels, American Society of Mechanical Engineers, Washington, DC, USA, 2016 V001T009A004-V001T009A004.

[34] S.H. Kim, H. Seon Ahn, J. Kim, M. Kaviany, M. Hwan Kim, Dynamics of water droplet on a heated nanotubes surface, Appl. Phys. Lett. 102 (23) (2013) 233901.

[35] G.C. Lee, J.Y. Kang, H.S. Park, K. Moriyama, S.H. Kim, M.H. Kim, Induced liquid–solid contact via micro/nano multiscale texture on a surface and its effect on the Leidenfrost temperature, Exp. Therm. Fluid Sci. 84 (2017) 156–164.

[36] W. Tong, L. Qiu, J. Jin, L. Sun, F. Duan, Unique lift-off of droplet impact on high temperature nanotube surfaces, Appl. Phys. Lett. 111 (9) (2017) 091605.

[37] M. Auliano, M. Fernandino, P. Zhang, C.A. Dorao, Water droplet impacting on overheated random Si nanowires, Int. J. Heat Mass Transf. 124 (2018) 307–318.

[38] M. Auliano, D. Auliano, M. Fernandino, P. Asinari, C.A. Dorao, Can wicking control droplet cooling? Langmuir (2019).

[39] H. Kim, B. Truong, J. Buongiorno, L.-W. Hu, On the effect of surface roughness height, wettability, and nanoporosity on Leidenfrost phenomena, Appl. Phys. Lett. 98 (8) (2011) 083121.

[40] C.T. Avedisian, J. Koplik, Leidenfrost boiling of methanol droplets on hot porous/ceramic surfaces, Int. J. Heat Mass Transf. 30 (2) (1987) 379–393.

[41] M. Fatehi, M. Kaviany, Analysis of levitation of saturated liquid droplets on permeable surfaces, Int. J. Heat Mass Transf. 33 (5) (1990) 983–994.

[42] N.R. Geraldi, G. McHale, B.B. Xu, G.G. Wells, L.E. Dodd, D. Wood, M.I. Newton, Leidenfrost transition temperature for stainless steel meshes, Mater. Lett. 176 (2016) 205–208.

[43] H.M. Kwon, J.C. Bird, K.K. Varanasi, Increasing Leidenfrost point using micro–nano hierarchical surface structures, Appl. Phys. Lett. 103 (20) (2013) 5.

[44] C. Kruse, T. Anderson, C. Wilson, C. Zuhlke, D. Alexander, G. Gogos, S. Ndao, Extraordinary shifts of the Leidenfrost temperature from multiscale micro/nanostructured surfaces, Langmuir 29 (31) (2013) 9798–9806.

[45] N. Farokhnia, S.M. Sajadi, P. Irajizad, H. Ghasemi, Decoupled hierarchical structures for suppression of Leidenfrost phenomenon, Langmuir 33 (10) (2017) 2541–2550.

[46] B.T. Ng, Y.M. Hung, M.K. Tan, Suppression of the Leidenfrost effect via low frequency vibrations, Soft Matter 11 (4) (2015) 775–784.

[47] B.T. Ng, Y.M. Hung, M.K. Tan, Acoustically-controlled Leidenfrost droplets, J. Colloid Interface Sci. 465 (2016) 26–32.

[48] F. Celestini, G. Kirstetter, Effect of an electric field on a Leidenfrost droplet, Soft Matter 8 (22) (2012) 5992–5995.

[49] A. Shahriari, J. Wurz, V. Bahadur, Heat transfer enhancement accompanying Leidenfrost state suppression at ultrahigh temperatures, Langmuir 30 (40) (2014) 12074–12081.

[50] A. Shahriari, S. Das, V. Bahadur, R.T. Bonnecaze, Analysis of the instability underlying electrostatic suppression of the Leidenfrost state, Phys. Rev. Fluids 2 (3) (2017) 11.

[51] O. Ozkan, A. Shahriari, V. Bahadur, Electrostatic suppression of the Leidenfrost state using AC electric fields, Appl. Phys. Lett. 111 (14) (2017) 5.

[52] Z. Tamura, Y. Tanasawa, Evaporation and combustion of a drop contacting with a hot surface, in: Symposium (International) on Combustion, Elsevier, 1958, pp. 509–522.

[53] C. Gerardi, J. Buongiorno, L.-W. Hu, T. McKrell, Study of bubble growth in water pool boiling through synchronized, infrared thermometry and high-speed video, Int. J. Heat Mass Transf. 53 (19–20) (2010) 4185–4192.

[54] A. Sur, Y. Lu, C. Pascente, P. Ruchhoeft, D. Liu, Pool boiling heat transfer enhancement with electrowetting, Int. J. Heat Mass Transf. 120 (2018) 202–207.

[55] B.S. Gottfried, C.J. Lee, K.J. Bell, The Leidenfrost phenomenon: film boiling of liquid droplets on a flat plate, Int. J. Heat Mass Transf. 9 (11) (1966) 1167–1188.

[56] A.L. Biance, C. Clanet, D. Quere, Leidenfrost drops, Phys. Fluids 15 (6) (2003) 1632–1637.

[57] D. Quere, Leidenfrost dynamics, in: S.H. Davis, P. Moin (Eds.), Annual Review of Fluid Mechanics, 45, Annual Reviews, Palo Alto, 2013, pp. 197–215.

[58] V.P. Carey, Liquid-Vapor Phase-Change Phenomena, Second ed., 2008.

[59] P.A. Raghupathi, S.G. Kandlikar, Bubble growth and departure trajectory under asymmetric temperature conditions, Int. J. Heat Mass Transf. 95 (2016) 824–832.

[60] V.S. Nikolayev, D. Chatain, Y. Garrabos, D. Beysens, Experimental evidence of the vapor recoil mechanism in the boiling crisis, Phys. Rev. Lett. 97 (18) (2006).

[61] V.S. Nikolayev, D.A. Beysens, Boiling crisis and non-equilibrium drying transition, Europhys. Lett. 47 (3) (1999) 345–351.

[62] T.B. Jones, J.D. Fowler, Y.S. Chang, C.J. Kim, Frequency-based relationship of electrowetting and dielectrophoretic liquid microactuation, Langmuir 19 (18) (2003) 7646–7651.

[63] D. Quere, M. Reyssat, Non-adhesive lotus and other hydrophobic materials, Philos. Trans. R. Soc. A-Math. Phys. Eng. Sci. 366 (1870) (2008) 1539–1556.

[64] Y.S. Nanayakkara, D.W. Armstrong, A liquid drop RC filter apparatus for detection, Anal. Bioanal. Chem. 401 (9) (2011) 2669.

[65] B. Shapiro, H. Moon, R.L. Garrell, C.-J.C. Kim, Equilibrium behavior of sessile drops under surface tension, applied external fields, and material variations, J. Appl. Phys. 93 (9) (2003) 5794–5811.

[66] C.B. Moore, B. Vonnegut, Measurements of the electrical conductivities of air over hot water, J. Atmospheric Sci. 45 (5) (1988) 885–890.

[67] J.K. Srivastava, M. Prasad, J.B. Wagner Jr., Electrical conductivity of silicon dioxide thermally grown on silicon, J. Electrochem. Soc. 132 (4) (1985) 955–963.

[68] H.H. Woodson, J.R. Melcher, Field description of magnetic and electric forces (Chapter 8), in: Electromechanical Dynamics - Part 2, 1968, pp. 418–478.

[69] J.A. Stratton, Stress and energy (chapter 2), in: Electromagnetic Theory, 2015, pp. 97–103.

[70] J.R. Melcher, Stress tensors and surface forces, A Tutorial on Induced Electro-hydrodynamic Forces, 1968.

[71] G.I. Taylor, The instability of liquid surfaces when accelerated in a direction perpendicular to their planes. I, Proc. R. Soc. Lond. Ser. A. Mathem. Phys. Sci. 201 (1065) (1950) 192–196.

[72] N. Zuber, On the stability of boiling heat transfer, Trans. Am. Soc. Mech. Eng. (1958) 80.

[73] P.J. Berenson, Film-boiling heat transfer from a horizontal surface, J. Heat Transf. 83 (3) (1961) 351–356.

[74] D.Y. Hsieh, Interfacial stability with mass and heat transfer, Phys. Fluids 21 (5) (1978) 745–748.

[75] S.P. Ho, Linear Rayleigh-Taylor stability of viscous fluids with mass and heat transfer, J. Fluid Mech. 101 (1980) 111–128.

[76] K. Adhamkhodaparast, M. Kawaji, B.N. Antar, The Rayleigh–Taylor and Kelvin–Helmholtz stability of a viscous liquid–vapor interface with heat and mass transfer, Phys. Fluids 7 (2) (1995) 359–364.

[77] B.J. Kim, J.H. Lee, K.D. Kim, Improvements of critical heat flux models for pool boiling on horizontal surfaces using interfacial instabilities of viscous potential flows, Int. J. Heat Mass Transf. 93 (2016) 200–206.

[78] J. Berghmans, Electrostatic fields and the maximum heat flux, Int. J. Heat Mass Transf. 19 (7) (1976) 791–797.

[79] P. Di Marco, W. Grassi, Saturated pool boiling enhancement by means of an electric field, J. Enhanced Heat Transf. 1 (1) (1994) 99–114.

[80] M. Uemura, S. Nishio, I. Tanasawa, Enhancement of Pool Boiling Heat Transfer by Static Electric Field, in, Begel House Inc.

[81] J.S. Sharp, D.J. Farmer, J. Kelly, Contact angle dependence of the resonant frequency of sessile water droplets, Langmuir 27 (15) (2011) 9367–9371.

[82] G. McHale, S.J. Elliott, M.I. Newton, D.L. Herbertson, K. Esmer, Levitation-free vibrated droplets: resonant oscillations of liquid marbles, Langmuir 25 (1) (2009) 529–533.

[83] F. Mugele, J.-C. Baret, Electrowetting: from basics to applications, J. Phys. Condens. Matter 17 (28) (2005) R705.